Title

Oxygen isotope geochemistry of Laurentide ice-sheet meltwater across Termination I

Authors

Vetter, Lael
Spero, Howard J
Eggins, Stephen M
et al.

Publication Date

2017-12-01

DOI

10.1016/j.quascirev.2017.10.007

Peer reviewed

Quaternary Science Reviews 178 (2017) 102–117

Contents lists available at ScienceDirect

Quaternary Science Reviews

journal homepage: www.elsevier.com/locate/quascirev

Oxygen isotope geochemistry of Laurentide ice-sheet meltwater across Termination I

Lael Vetter [a, *], Howard J. Spero [a], Stephen M. Eggins [b], Carlie Williams [c], Benjamin P. Flower [c]

[a] Department of Earth and Planetary Sciences, University of California Davis, Davis, CA 95616, USA
[b] Research School of Earth Sciences, The Australian National University, Canberra 0200, ACT, Australia
[c] College of Marine Sciences, University of South Florida, St. Petersburg, FL 33701, USA

ARTICLE INFO

Article history:
Received 3 April 2017
Received in revised form
1 October 2017
Accepted 4 October 2017

ABSTRACT

We present a new method that quantifies the oxygen isotope geochemistry of Laurentide ice-sheet (LIS) meltwater across the last deglaciation, and reconstruct decadal-scale variations in the $\delta^{18}O$ of LIS meltwater entering the Gulf of Mexico between ~18 and 11 ka. We employ a technique that combines laser ablation ICP-MS (LA-ICP-MS) and oxygen isotope analyses on individual shells of the planktic foraminifer *Orbulina universa* to quantify the instantaneous $\delta^{18}O_{water}$ value of Mississippi River outflow, which was dominated by meltwater from the LIS. For each individual *O. universa* shell, we measure Mg/Ca (a proxy for temperature) and Ba/Ca (a proxy for salinity) with LA-ICP-MS, and then analyze the same *O. universa* for $\delta^{18}O$ using the remaining material from the shell. From these proxies, we obtain $\delta^{18}O_{water}$ and salinity estimates for each individual foraminifer. Regressions through data obtained from discrete core intervals yield $\delta^{18}O_w$ vs. salinity relationships with a y-intercept that corresponds to the $\delta^{18}O_{water}$ composition of the freshwater end-member. Our data suggest that from 15.5 through 14.6 ka, estimated $\delta^{18}O_w$ values of Mississippi River discharge from discrete core intervals range from −11‰ to −21‰ VSMOW, which is consistent with $\delta^{18}O$ values from both regional precipitation and the low-elevation, southern margin of the LIS. During the Bølling and Allerød (14.0 through 13.3 ka), estimated $\delta^{18}O_w$ values of Mississippi River discharge from discrete core intervals range from −22‰ to −38‰ VSMOW. These values suggest a dynamic melting history of different parts of the LIS, with potential contributions to Mississippi River outflow from both the low-elevation, southern margin of the LIS and high-elevation, high-latitude domes in the LIS interior that were transported to the ablation zone. Prior to ~15.5 ka, the $\delta^{18}O_{water}$ value of the Mississippi River was similar to that of regional precipitation or low-latitude LIS meltwater, but the Ba concentration in the Mississippi basin was affected by changes in weathering within the watershed, complicating Ba-salinity relationships in the Gulf of Mexico. After 13 ka, our data suggest Mississippi River outflow did not influence surface salinity above our Gulf of Mexico Orca Basin core site. Rather, we hypothesize that open ocean conditions prevailed as sea level rose and the paleo-shoreline at the southern edge of North America retreated northward.

1. Introduction

The evolution and demise of continental ice sheets is intrinsically linked to variations in sea level (Carlson and Clark, 2012; Deschamps et al., 2012; Gregoire et al., 2012; Lambeck et al., 2002) and ocean circulation (Clark et al., 2001; Thornalley et al., 2010) on glacial/interglacial timescales. Numerical models provide insight into the spatial and temporal patterns of the history of continental ice sheets such as the Laurentide Ice Sheet (LIS) during the last glacial cycle. However, ice-sheet thickness remains one of the greatest sources of uncertainty in constraining ice-sheet dynamics (Ullman et al., 2014), and modeled thicknesses for the LIS vary depending on model selection (Argus et al., 2014; Clark et al., 1994; Gregoire et al., 2012; Kleman et al., 2002; Lambeck et al., 2002; Marshall et al., 2000; Peltier et al., 2015; Rutt et al., 2009; Tarasov and Peltier, 2004). Oxygen isotope variations within an

* Corresponding author. Current address: Department of Geosciences, University Arizona, Tucson, AZ 85721, USA.
E-mail address: lael.vetter@gmail.com (L. Vetter).

https://doi.org/10.1016/j.quascirev.2017.10.007
0277-3791/

ice sheet are controlled by temperature, latitude, and altitude (Bowen and Wilkinson, 2002; Oerlemans, 1982), so the geochemical heterogeneity of the ice within an ice sheet preserves a record of physical parameters that affect Rayleigh fractionation, including ice-sheet elevation. During inception and growth of the LIS, southward deflection of westerly storm tracks over North America (Oster et al., 2015) may have had an effect on the isotopic value of precipitation over the LIS. The distribution of $\delta^{18}O$ values within an ice sheet is also dependent on ice flow subsequent to precipitation. Specific to this study, the oxygen isotope value of meltwater ($\delta^{18}O_w$) draining a continental ice sheet during its demise is directly related to the regions that are melting. Hence, quantifying meltwater $\delta^{18}O_w$ derived from ice sheets has the potential to yield valuable information on past precipitation temperatures, water vapor sources, and ice-sheet dynamics.

Oxygen isotope analyses of marine sedimentary records proximal to LIS meltwater outflow offer the most direct evidence of the isotopic evolution of the LIS, and help to constrain the location and timing of routing of meltwater (e.g., Aharon, 2003, 2006; Broecker et al., 1989; Carlson, 2009; Carlson et al., 2007; Flower et al., 2004; Hill et al., 2006; Hoffman et al., 2012; Keigwin et al., 1991; Williams et al., 2012). However, mixing models of meltwater contributions to the ocean typically assume a constant $\delta^{18}O_w$ value for the LIS (−25 or −35‰; Aharon, 2006; Carlson, 2009; Carlson et al., 2007; Hill et al., 2006; Obbink et al., 2010), and do not attempt to incorporate the complex spatial heterogeneity in $\delta^{18}O_w$ observed in modern continental ice sheets (Masson-Delmotte et al., 2008; Vinther et al., 2009). Attempts to estimate the oxygen isotope composition of parts of the LIS have used measurements of remnant ice such as the Barnes Ice Cap (Hooke, 1976; Hooke and Clausen, 1982), Pleistocene-age groundwater (Hooke and Clausen, 1982; Remenda et al., 1994) and preserved ice wedges (Kotler and Burn, 2000); as well as indirect proxies from subglacial carbonates (Refsnider et al., 2012, 2014) and proglacial lakes (Birks et al., 2007; Buhay and Betcher, 1998; Last et al., 1994; Moore et al., 2000).

Simple numerical models of oxygen isotope distribution within the LIS are consistent with these values (Sima et al., 2006). In addition, global circulation models (GCMs) that incorporate Rayleigh-type fractionation (Carlson et al., 2008a; LeGrande et al., 2006; Pausata et al., 2011; Risi et al., 2010; Ullman et al., 2014; Werner et al., 2011; Yoshimura et al., 2008) can estimate oxygen isotope heterogeneity in precipitation. These types of models offer an alternative approach to modeling ice-sheet heterogeneity, and recent efforts have begun to link modeled $\delta^{18}O_w$ of Pleistocene precipitation with LIS-derived groundwater measurements (Ferguson and Jasechko, 2015). However, linking the timing and causal relationships between ice-sheet dynamics and marine records of ice-sheet meltwater remains challenging. The provenance of meltwater source(s) on the LIS are poorly constrained and difficult to identify (Flower et al., 2011), as are the volume and $\delta^{18}O_w$ of freshwater outflow. Quantifying the $\delta^{18}O_w$ evolution of meltwater during deglaciation could thus provide a powerful isotopic tool for ice-sheet reconstructions.

Early reconstructions of meltwater histories from planktic foraminifer geochemistry (e.g., Kennett and Shackleton, 1975; Leventer et al., 1982) were limited by the use of a single proxy, the $\delta^{18}O$ value of foraminiferal calcite ($\delta^{18}O_c$), and the ambiguity associated with the dependence of $\delta^{18}O_c$ not only on temperature but on $\delta^{18}O_{sw}$, which varies with salinity. Foraminifer $\delta^{18}O_c$ records from multiple shells in a single sample provide a qualitative measure of the geochemistry of Mississippi River input into the Gulf of Mexico, which is observed as a large decrease in shell $\delta^{18}O_c$. Studies have used these data to estimate the $\delta^{18}O_w$ of a freshwater endmember in meltwater runoff (Flower et al., 2004; Hill et al., 2006; Williams et al., 2012) using simple mixing models. However, using these previously collected data sets, one cannot directly compute meltwater $\delta^{18}O_w$ without *a priori* knowledge or assumptions about average seawater $\delta^{18}O_{sw}$ and salinity over the coring site. To date there are no direct methods to quantify the $\delta^{18}O_w$ value of LIS meltwater that flowed into the Gulf of Mexico.

Research on LIS meltwater geochemistry in the above studies utilized the classic technique of combining numerous foraminifer shells into a single $\delta^{18}O_c$ measurement, thereby producing an average signal for a core interval. This averaging technique conceals the intraspecific variability contained in a population of foraminifers, which during meltwater intervals can exceed 4‰ between individual shells (Spero and Williams, 1990). These authors suggested that the $\delta^{18}O_c$ range reflected reduced salinities in the upper water column from mixing with a proximate source of ^{18}O-depleted glacial meltwater. Such studies demonstrate that an additional dimension of hydrographic information can be recovered when a suite of individual foraminifer shells are analyzed (Billups and Spero, 1996; Ford et al., 2015; Koutavas et al., 2006; Koutavas and Joanides, 2012; Rustic et al., 2015).

In marine environments, salinity (S) and $\delta^{18}O_{sw}$ are both controlled by the balance between evaporation and freshwater inputs such as precipitation and riverine outflow, and as a result S and $\delta^{18}O_{sw}$ covary in the ocean (Fig. S-1; Fairbanks et al., 1992). Because mixing between seawater and a freshwater source produces a two end-member relationship, the y-intercept (where $S = 0$) of the salinity-$\delta^{18}O_{sw}$ relationship yields the $\delta^{18}O_w$ of the regional freshwater endmember. For regions where salinity changes are primarily controlled by the influx of glacial meltwater, the y-intercept becomes an integrated mass balance of $\delta^{18}O_w$ between ice-sheet melt and rainfall sources that contributed to fluvial runoff. If such regressions can be reconstructed for discrete time periods during meltwater intervals, it may be possible to reconstruct dynamic changes in the geographic sources of ice sheet melt via analysis of river outflow geochemistry.

In this paper, we apply a novel geochemical approach to quantifying the instantaneous $\delta^{18}O_w$ value of Mississippi River outflow that was dominated by meltwater from the LIS during the last deglaciation. We use geochemical measurements of individual planktic foraminifers from Orca Basin core MD02-2550 (26.95°N, 91.35°W, 2245 m) in the Gulf of Mexico (Fig. 1). We combine measured $\delta^{18}O$ and Mg/Ca with Ba/Ca (an independent salinity proxy) to reconstruct $\delta^{18}O_w$-salinity regression relationships, which generate estimates of meltwater $\delta^{18}O_w$ at the Mississippi River outflow. We apply this technique to 31 discrete core intervals during the last deglaciation (~17.5–12 ka). Results suggest that the $\delta^{18}O_w$ of LIS meltwater in the Mississippi River was highly variable over short timescales, implying a complex melting history and rapid switching of meltwater sources between different regions of the LIS.

2. Methodology

2.1. Planktic foraminifer ecology and geochemistry

The planktic foraminifer *Orbulina universa* offers several advantages over other species for reconstructing a range of near-surface hydrographic conditions. First, the relationships for $\delta^{18}O_c$-temperature, Mg/Ca-temperature, and Ba/Ca_{shell}-Ba/Ca_{sw} for this species have been characterized and quantified in numerous laboratory culture experiments (Bemis et al., 1998; Hönisch et al., 2011; Lea et al., 1999; Russell et al., 2004), thereby minimizing potential errors that might arise from using multi-species calibrations. *Orbulina universa* also secretes a large spherical shell that thickens radially over a short period (3–10 days; Spero, 1988) and is typically >350 μm in diameter and >20 μg (Russell et al., 2004;

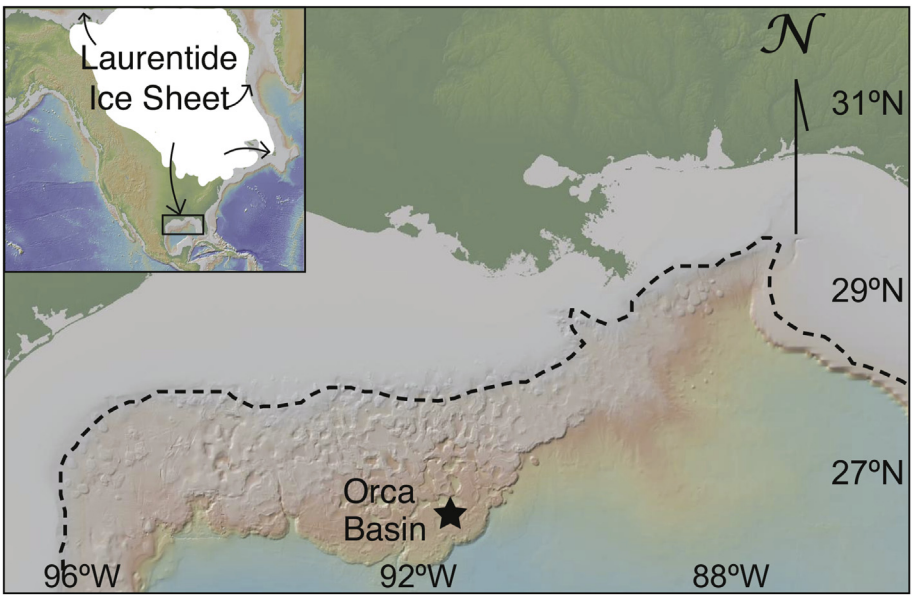

Fig. 1. Location of Orca Basin in the Gulf of Mexico with 15 ka paleo-shoreline (dashed line locates bathymetric contour at 100 m depth below modern sea-level (after Aharon, 2006)). Inset map shows likely outlets of Laurentide Ice Sheet melt (after Licciardi et al., 1999).

Wolf-Gladrow et al., 1999). As a result, fragments of the spherical shell from a single individual contain the same geochemical and paleoenvironmental information without concern for ontogenetic variability (Fehrenbacher et al., 2015). Furthermore, the large shell mass permits researchers to measure the geochemistry of multiple fragments using different analytical instruments (Vetter et al., 2013a).

Orbulina universa has a broad temperature and salinity tolerance (9-30 °C, 23–46 psu; Bé et al., 1973; Bijma et al., 1990), and the depth habitat of this species spans the photic zone (Bé, 1977; Fairbanks et al., 1982). Therefore, a suite of *O. universa* shells from a single core interval has the potential to record a wide range of contemporaneous environmental conditions throughout the upper water column. These characteristics often make *O. universa* unsuitable for reconstructing near-surface paleoceanographic conditions in some applications, but are ideal for capturing a range of salinity and $\delta^{18}O_w$ values within the mixed layer and upper thermocline that are required to generate a robust $\delta^{18}O_w$-salinity relationship.

The $\delta^{18}O_c$ of foraminiferal calcite is dependent on both temperature and the $\delta^{18}O_w$ from which the foraminifer calcified (Bemis et al., 1998, and references therein). Laboratory culture experiments with live *O. universa* grown under low light produced the empirical calibration (Bemis et al., 1998):

$$T(°C) = 16.5(\pm0.2) - 4.80(\pm0.16)*(\delta^{18}O_c - (\delta^{18}O_w - 0.27)) \quad (1)$$

Paleotemperature calculations based solely on $\delta^{18}O_c$ are complicated by the dependence of this proxy on $\delta^{18}O_w$, which varies regionally, with depth in the ocean, and over glacial-interglacial timescales. The Mg/Ca ratio preserved in foraminiferal calcite is controlled primarily by temperature, thereby providing a geochemical thermometer that is independent of $\delta^{18}O_c$. Laboratory calibration of Mg/Ca versus temperature have been published for *O. universa* (Lea et al., 1999; Russell et al., 2004), with confirmation from sediment trap studies (Anand et al., 2003). Here we use the Mg/Ca-temperature relationship of Russell et al. (2004):

$$\ln Mg/Ca = -0.162(\pm0.295) + 0.096(\pm0.014)*T \quad (2)$$

where Mg/Ca is measured in mmol mol^{-1} and T is measured in °C.

Calculated temperatures from shell Mg/Ca (eq. (2)) have been used in conjunction with $\delta^{18}O_c$ from the same core intervals to compute the $\delta^{18}O$ of seawater ($\delta^{18}O_{sw}$) during calcification (Flower et al., 2004; Hill et al., 2006; Hoffman et al., 2012; Lea et al., 2000; Obbink et al., 2010; Schmidt et al., 2004; Williams et al., 2012). Several studies have interpreted the residual $\delta^{18}O_{sw}$ value in terms of relative salinity changes, variations in the hydrologic cycle, or surface water hydrography (Carlson et al., 2007; Hoffman et al., 2012; Obbink et al., 2010; Schmidt et al., 2004, 2006; Thornalley et al., 2011). However, the direct conversion of $\delta^{18}O_{sw}$ to salinity is not possible unless a local $\delta^{18}O_{sw}$-salinity relationship is known or can be estimated.

2.2. Reconstructing paleosalinity

In the open ocean, $\delta^{18}O_{sw}$ and salinity are controlled by evaporation and precipitation, and the $\delta^{18}O_w$ value of precipitation over the open-ocean is typically close to that of VSMOW. In contrast, marine $\delta^{18}O_{sw}$ near continental margins influenced by major rivers are primarily influenced by the $\delta^{18}O_w$ value of riverine outflow. Riverine $\delta^{18}O_w$ values, in turn, are governed by seasonal precipitation, evaporation, Rayleigh fractionation processes, and the relative contributions of different watersheds in complex systems (Bowen and Wilkinson, 2002). During the last deglaciation, the $\delta^{18}O_w$ value of Mississippi River discharge into the Gulf of Mexico was determined by two factors: a $\delta^{18}O$ signal of continental precipitation integrated over the watershed, and seasonal contributions of meltwater from the melting LIS. The deglacial rate of freshwater influx from seasonally melting ice sheets has been estimated at 14,000 km^3 yr^{-1} (Fairbanks, 1989) during Meltwater Pulse 1a (MWP-1a), an interval of particularly rapid sea-level rise (40 mm yr^{-1}; Deschamps et al., 2012); for comparison, this is 20x the modern annual average Mississippi River discharge of ~700 km^3 yr^{-1} (Allison et al., 2012). Based on these estimates, meltwater from the LIS was a dominant component of Mississippi River discharge during parts of the deglaciation (Fairbanks et al., 1992). Here we assume that variations in the volume of continental precipitation in the Mississippi River drainage basin, and

variations in the isotopic composition of that precipitation, were negligible during the deglaciation.

The concentration of dissolved barium (Ba) in rivers varies as a function of basin lithology, geometry, and rate of runoff, and can range from ~100 to 600 nmol l^{-1} (Coffey et al., 1997). Conversely, [Ba] is very low (e.g., ~33–40 nmol l^{-1}) in the open ocean (Lea and Boyle, 1991; Lea and Spero, 1994). The concentration of fluvial-derived Ba in estuarine mixing zones increases during mixing at low salinities (5–15 psu (practical salinity units)), as barium desorbs from suspended particulate matter, up to 350–500 nmol l^{-1} (Coffey et al., 1997; Hanor and Chan, 1977). The behavior of Ba at low, estuarine salinities is non-conservative, but conservative mixing of Ba between brackish estuarine salinities and open marine waters is observed at salinities >15 psu (Coffey et al., 1997; Guay and Falkner, 1997). The Ba/Ca ratio of seawater can therefore be used to quantify salinities >15–20 psu.

Several recent studies have demonstrated that Ba/Ca_{shell} in foraminifera from marine environments proximal to riverine outflow can be used as an independent proxy for reconstructing paleosalinity (Hall and Chan, 2004; Plewa et al., 2006; Sprovieri et al., 2008; Weldeab et al., 2007). The relationship between riverine Ba/Ca and salinity varies geographically. Weldeab et al. (2007) showed that Niger River Ba/Ca differs from the Amazon (Boyle, 1976) and the Ganges-Brahmaputra (Fig. S-2a; Carroll et al., 1993). Planktic foraminifers incorporate Ba into shell calcite in direct proportion to the [Ba] in seawater (Lea and Spero, 1992, 1994), and shell Ba/Ca is independent of changes in seawater carbonate chemistry, temperature, or salinity (Hönisch et al., 2011):

$$Ba/Ca_{shell} = 0.149(\pm 0.05)^{*}Ba/Ca_{sw} \quad (3)$$

To generate a [Ba] vs. salinity relationship for the mixing between Mississippi River outflow and the Gulf of Mexico, we use a modern data set of >300 paired measurements of [Ba] and salinity from the entire Mississippi-Atchafalaya River system, across a range of salinities (Hanor and Chan, 1977; Joung and Shiller, 2014). We convert Ba/Ca_{sw} to Ba/Ca_{shell} (expressed in μmol mol^{-1}) using eq. (3) for data points with S > 15 psu, to avoid the non-conservative mixing behavior of Ba at estuarine salinities <15 psu (Coffey et al., 1997; Hanor and Chan, 1977). The resulting local salinity-Ba/Ca_{shell} relationship (Fig. S-2b) for Mississippi River mixing into the Gulf of Mexico is:

$$S\,(psu) = 36.35(\pm 0.008) - 1.734(\pm 0.002)^{*}(Ba/Ca_{shell})\ (r^2 = 0.82) \quad (4)$$

We use this relationship to convert measured *O. universa* Ba/Ca_{shell} into S.

2.3. Materials and analyses

For this study, we sampled 31 core intervals at 0.5 or 1 cm spacing resolution from Gulf of Mexico core MD02-2550 (26.95°N, 91.35°W, 2245 m) collected in the Orca Basin. These samples consist of adjacent core intervals from 9 discrete time slices during the last deglaciation (17.5–12 ka; Fig. 2), and include samples from during the early deglaciation (>17.0 ka; time slice ED), Heinrich Stadial 1 (17.0–14.7 ka; time slices H_a, H_b, and H_c), the Bølling-Allerød Warm Periods (14.7–13.0 ka; time slices B_a, B_b, B_c, and B_d), and during the Younger Dryas (12.9–11.8 ka; time slice YD). The age model for this core is based on 35 radiocarbon dates spaced ~10 cm apart, with the interpolated age model based on the assumption of a constant sedimentation rate between tie points. From 14.7 to 10.7 ka, the average amount of time represented by 1 cm of sediment is ~28 yr, and prior to 14.7 ka is ~24 yr (Williams et al., 2010). The variability measured between individual foraminifera in 0.5 cm or 1 cm core intervals therefore represents averaging of decadal-scale processes. We also selected a late Holocene interval (20–22 cm depth) from nearby Orca Basin core MD02-2551 (26.95°N, 91.35°W, 2248 m) to ground-truth the technique on shells not influenced by Mississippi River outflow.

From each core interval, 15–35 fossil *O. universa* were randomly selected from the >350 μm sieve fraction. Individual *O. universa* were sonicated in methanol for 5–10 s and then mechanically split into several fragments using a razor blade. If sediment was still present inside shells following sonication, it was mechanically removed using a small brush (size 0000) after the shell was split. Fragments of shell calcite were not subjected to further cleaning procedures such as oxidative or reductive cleaning. The largest fragment of each shell (10–40 μg) was roasted *in vacuo* for 30 min at 375°C prior to stable isotopic analysis. For fragments >20 μg, $\delta^{18}O_c$ analyses were conducted with a Fisons Optima dual inlet isotope ratio mass spectrometer (IRMS) using 105% H_3PO_4 in a common acid bath at 90°C. For samples <20 μg, analyses were conducted using a MicroMass Isoprime dual inlet IRMS with Isoprime multicarb and Gilson autosampler, where samples were reacted in individual vials with 105% H_3PO_4 at 90°C. All $\delta^{18}O_c$ analyses were performed in the Stable Isotope Laboratory, Department of Earth and Planetary Sciences, at the University of California-Davis. Data were standardized to VPDB using a Carrara marble internal laboratory standard (UCD-SM92) with overall analytical precision of 0.06‰ and 0.03‰ (±1 SD) for $\delta^{18}O_c$ and $\delta^{13}C$, respectively. Analytical runs were typically composed of 30 samples and 7 standards; all standards were pre-weighed to bracket the mass range of the samples.

A small remaining fragment from each individual *O. universa* was analyzed for Mg/Ca and Ba/Ca. Individual shell fragments were analyzed using a pulsed 193 nm ArF Excimer laser ablation (LA) system with a dual-volume sampling chamber, ablated in depth profile from shell interior to exterior. Each laser pulse ablated ~0.1 μm of shell material, which was analyzed on a quadrupole inductively coupled plasma mass spectrometer (ICP-MS). Approximately half of the LA-ICP-MS analyses were conducted at the Research School of Earth Sciences, Australian National University, using a dual-volume ANU HelEx sample chamber coupled to an Agilent 7500s ICP-MS. Remaining analyses were conducted in the Department of Earth and Planetary Sciences, University of California, Davis, using a Photon Machines 193 nm Excimer laser with HeLex dual-volume sample chamber coupled to an Agilent 7700x ICP-MS (Fig. S-3). The LA-ICP-MS operating conditions for both laboratories are summarized in Table 1.

Quadrupole ICP-MS analyses measured ^{24}Mg, ^{25}Mg, ^{27}Al, ^{43}Ca, ^{44}Ca, ^{55}Mn, ^{88}Sr, and ^{138}Ba; dwell times for each mass are in Table 1. Offline data reduction followed the procedure of Eggins et al. (2003) and consisted of initial screening for outliers, subtraction of mean background intensities, internal standardization to $^{43}Ca/^{44}Ca$, and external standardization to a NIST 610 standard glass which was measured every ~20 samples. Three or more replicate profiles were ablated through each shell fragment. Quality control on ablated profiles included screening and exclusion of initial high counts of Al/Ca from surface contamination, and an observed initial anomalous associated high metal/calcium (Me/Ca) ratio (Fig. S-3; Vetter et al., 2013b). This initial high Me/Ca appears on depth profiles of both uncleaned shells and shells that have undergone reductive and oxidative cleaning, and is interpreted to be an artifact of the laser ablation process (Vetter et al., 2013b). A total of 6% of individual shells analyzed were culled from the full dataset (41 out of 668 specimens). Sample data rejection was based on a number of criteria (Fig. S-4): 1) Al/Ca >0.5 mmol mol^{-1}, indicating sedimentary contamination; 2) variable or heterogeneous intrashell Ba/Ca, which should be constant through a shell (Vetter et al., 2013a);

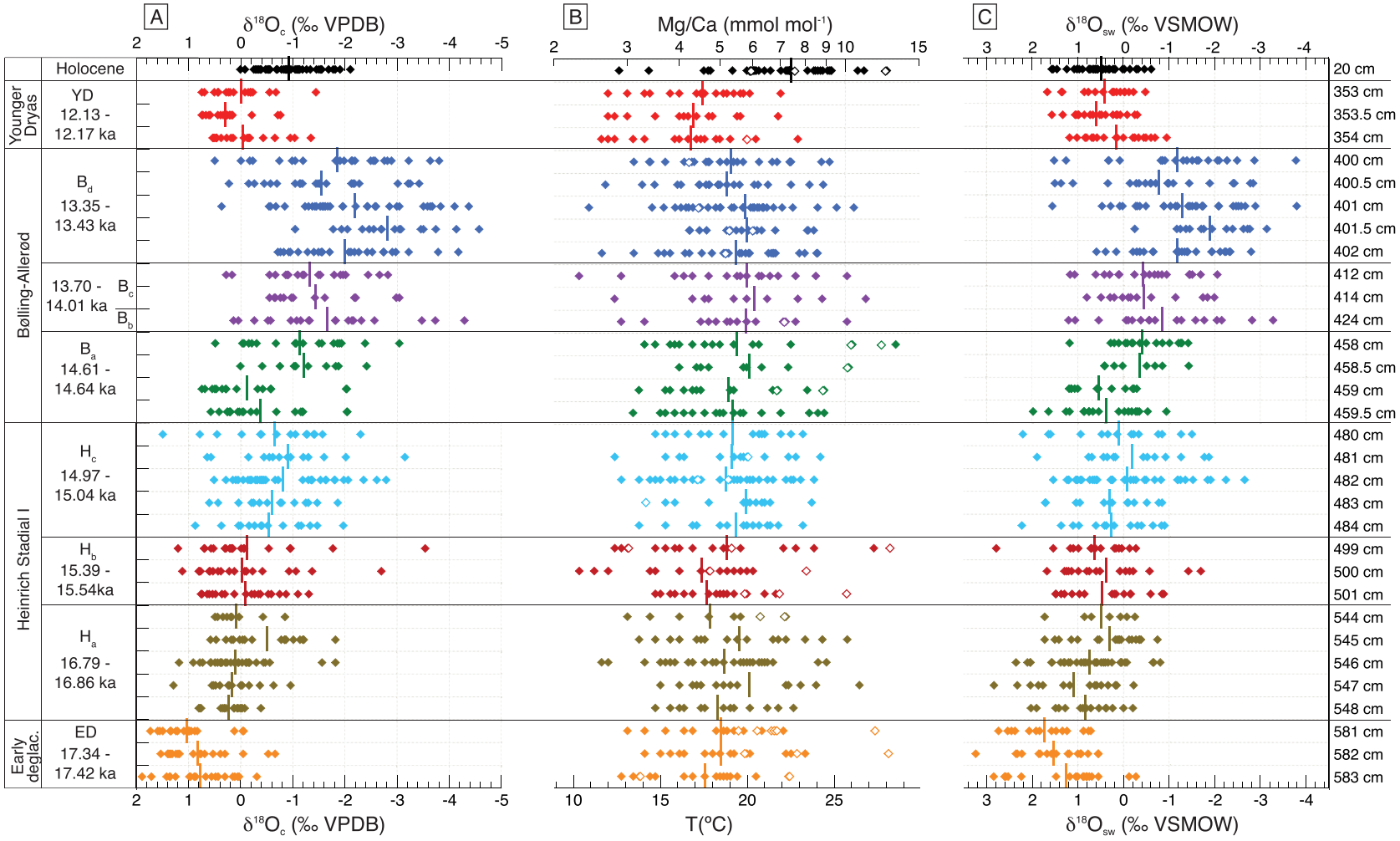

Fig. 2. A) $\delta^{18}O_c$ from individual *O. universa*. Color groups delineate adjacent 0.5 or 1 cm core intervals in discrete time slices (letter designations). The age model follows that of Williams et al. (2012). **B)** Measured Mg/Ca (mmol mol^{-1}) for each specimen in **(A)**, with corresponding temperatures (°C) calculated using eq. (2) from Russell et al. (2004). Open symbols identify LA-ICP-MS analyses that were culled from the final data set during LA-ICP-MS data screening and quality control. **(C)** Calculated $\delta^{18}O_{sw}$ for each specimen using the Bemis et al. (1998) low-light relationship (eq. (1)). Note that $\delta^{18}O_{sw}$ data are not corrected for ice volume change between time intervals. (For interpretation of the references to colour in this figure legend, the reader is referred to the web version of this article.)

Table 1
Laser ablation ICP-MS operating parameters at UC Davis and the Australian National University.

	ANU	UCD
ArF 193 nm Excimer Laser	Helex sampling chamber	Photon Machines
Energy density (fluence)	4 J cm^{-2}	1-3 J cm^{-2}
He gas flow	0.5 L min^{-1}	1.05 L min^{-1}
Laser repetition rate	4 Hz	5 Hz
Laser spot size	35 μm	30 μm
Quadrupole ICP-MS	Agilent 7500s	Agilent 7700x
ICP forward power	1300 W	1500 W
$^{232}Th^{16}O^{+}/^{232}Th^{+}$	<0.5%	<0.5%
Monitored masses (m/z) and isotope dwell time (ms)	^{24}Mg (30)	^{24}Mg (30)
	^{25}Mg (60)	^{25}Mg (60)
	^{27}Al (10)	^{27}Al (10)
	^{43}Ca (30)	^{43}Ca (30)
	^{44}Ca (30)	^{44}Ca (30)
	^{55}Mn (30)	^{55}Mn (30)
	^{88}Sr (30)	^{88}Sr (30)
	^{138}Ba (60)	^{138}Ba (60)
Core intervals analyzed	20-22 cm	20-22 cm
	400–402.5 cm	412–412.5 cm
	480–485 cm	414–414.5 cm
	544–549 cm	424–424.5 cm
		458–460 cm
		499–503 cm
		581–585 cm

or 3) Ba/Ca ratios >5 μmol mol^{-1}, which yield calculated salinity values < 27 psu that are outside the survival tolerance for *O. universa* (Bijma et al., 1990). After isolating the portion of each depth profile that reflects the biogenic signal (Fig. S-3), Mg/Ca and Ba/Ca in each profile was then averaged across the depth profile. Me/Ca ratios from multiple repeat depth profiles in the same shell were averaged to yield a single Me/Ca value for the individual foraminifer, and the standard deviation of these replicate depth profiles is the analytical error for Mg/Ca and Ba/Ca measurements on each individual shell. Thus, the uncertainty for LA-ICP-MS measurements is different for each individual foraminifera. Measured values and uncertainties are provided in Supplemental Data Table 1.

2.4. Calculating $\delta^{18}O$ of a freshwater end-member

For each individual *O. universa* shell, we combine IRMS-derived $\delta^{18}O_c$ (eq. (1)) with LA-ICP-MS-derived Mg/Ca (eq. (2)) to remove temperature from $\delta^{18}O_c$ and calculate $\delta^{18}O_w$ during calcification, with an error-propagated estimate of uncertainty on $\delta^{18}O_w$. From the initial measured Ba/Ca on the same individual shell, we decreased Ba/Ca_{shell} ratios by 13% to account for the effects of reductive and oxidative cleaning on Orca Basin shells (Vetter et al., 2013b), because we did not use reagent cleaning on shells prior to laser ablation analyses. We convert the resulting Ba/Ca_{shell} to salinity (S) using eq. (4), making the assumption that the Ba/Ca-S relationship for the modern Mississippi River is an appropriate estimate for deglacial runoff from the Mississippi River basin during all intervals analyzed in this study. From these geochemical data, we obtain paired $\delta^{18}O_{sw}$ and S values for each individual foraminifer. The uncertainties on $\delta^{18}O_{sw}$ and S for each individual, from analytical measurements and from proxy conversion to environmental parameters (equations (1)–(4)), were calculated following the error propagation methods of Rohling (2000). The $\delta^{18}O_{sw}$-S pairs from numerous individuals in a single core interval encompass a range of salinities and that can be regressed to yield a $\delta^{18}O_{sw}$ vs. S relationship for each core interval (~20 yr resolution).

To improve the confidence intervals on calculations of freshwater $\delta^{18}O_w$, we add an open-ocean S-$\delta^{18}O_{sw}$ endmember to the dataset for each core interval as an additional unweighted data point in each regression. We estimate the changing open-ocean end-member for $\delta^{18}O_{sw}$ and salinity during the deglaciation via several steps. First, modern $\delta^{18}O_{sw}$ values in the Gulf of Mexico vary between ~+1.1 and 1.3‰ (Joung and Shiller, 2014), and salinity is ~37 psu (Watanabe et al., 2001). Next, given a ~1.0‰ ice-volume enrichment of the global ocean between the LGM and late Holocene (Clark et al., 2009) and an ~1 psu saltier global ocean at the LGM (Adkins et al., 2002), we estimate open-ocean $\delta^{18}O_{sw}$ –S in the Gulf of Mexico at the LGM ($\delta^{18}O_{sw} = +2.2$‰; S = 38 psu). We then apply offsets in $\delta^{18}O_{sw}$ and S based on the eustatic sea-level curve and global ocean $\delta^{18}O$ of Clark et al. (2009), and calculate the $\delta^{18}O_{sw}$ for each time slice (Table 2). We use the same eustatic sea-level curve and assume a LGM-to-modern salinity decrease of 1 psu to estimate salinity for each time slice (Table 2). For each core interval, we include this estimate as an additional unweighted data point in the linear regression to determine the y-intercept $\delta^{18}O_w$ value of the freshwater end-member (Figs. S5 through S12). We apply a least-squares linear regression technique (York et al., 2004) that accounts for error estimates in both x and y (S and $\delta^{18}O_w$). Of the 31 deglacial time slices we analyzed, 18 yield significant relationships (Table 2). The y-intercept from each calculated relationship yields the $\delta^{18}O_w$ value of the freshwater endmember, which is dominated by LIS meltwater during seasonal melting of the ice sheet.

3. Results

3.1. $\delta^{18}O_c$, Mg/Ca, and $\delta^{18}O_w$

Measured $\delta^{18}O_c$ and Mg/Ca and reconstructed $\delta^{18}O_{sw}$ from individual *O. universa* are shown in Fig. 2. For Holocene core top specimens, $\delta^{18}O_c$ ranges from −2.10 to 0.01‰ VPDB and Mg/Ca ranges from 2.9 to 11.1 mmol mol^{-1}. These values correspond to estimated Holocene temperatures that range from 12.7°C to 26.8°C and calculated $\delta^{18}O_{sw}$ values that range from −0.61 to 1.57‰

Table 2
Summary of the 32 discrete core intervals analyzed in this study, including number of individual foraminifera analyzed per interval. Of 20 core intervals between 15.5 ka and 13.3 ka, 18 yield linear relationships between reconstructed $\delta^{18}O_{sw}$ and salinity for individual foraminifera. Linear regressions for each core interval include an open-ocean salinity and $\delta^{18}O_{sw}$ value for the Gulf of Mexico, scaled through the deglaciation, as an additional unweighted data point (see text for discussion). The y-intercept and S.E. for a linear regression of each core interval is the $\delta^{18}O_w$ of LIS meltwater, showing r^2 value for the regression, using a York fit (York et al., 2004). Core intervals from early in the deglaciation (ED), the earliest phase of Heinrich Stadial 1 (H_a), the Younger Dryas (YD), and the Holocene show no linear relationship between reconstructed $\delta^{18}O_{sw}$ and salinity for individual foraminifera.

Time slice	Age (ka)	Core interval depth (cm)	Orca Basin $\delta^{18}O_{sw}$ from *G. ruber* (w)*	*n*	Estimated salinity (psu) in open-ocean Gulf of Mexico	Estimated $\delta^{18}O_{sw}$ (‰) in open-ocean Gulf of Mexico	Linear regression of paired $\delta^{18}O_{sw}$ and S (this study), including open-ocean value for deglacial Gulf of Mexico		
							$\delta^{18}O_w$ (LIS)	1 S.E.	r^2
H	Holocene	20–22	–	40	37.00	1.20	no relationship		
YD	12.13–12.14	353–353.5	1.30	19	37.47	1.67	no relationship		
	12.14–12.16	353.5–354	1.25	20					
	12.16–12.17	354–354.5	1.03	19					
B_d	13.35–13.37	400–400.5	−1.85	23	37.54	1.74	no relationship		
	13.37–13.38	400.5–401	–	21			−38	8	0.46
	13.38–13.40	401–401.5	−2.60	33			−37	7	0.08
	13.40–13.41	401.5–402	−2.09	16			−31	8	0.56
	13.41–13.43	402–402.5	–	24			−30	8	0.28
B_c	13.70–13.75	412–412.5	−0.95	20	37.59	1.79	−32	8	0.53
	13.75–13.77	414–414.5	−0.83	13			−22	7	0.43
B_b	14.00–14.01	424–424.5	−1.23	19	37.65	1.85	−30	7	0.45
B_a	14.61–14.62	458–458.5	−1.64	17	37.73	1.93	−18	5	0.78
	14.62–14.63	458.5–459	−1.10	9			−21	8	0.65
	14.63–14.63	459–459.5	−0.03	13			−17	10	0.45
	14.63–14.64	459.5–460	−0.24	20			−21	9	0.3
H_c	14.97–14.98	480–481	−1.04	15	37.77	1.97	−17	5	0.43
	14.98–15.00	481–482	−1.18	14			−17	5	0.34
	15.00–15.01	482–483	−1.42	37			−19	3	0.58
	15.01–15.03	483–484	−0.51	13			−12	5	0.44
	15.03–15.04	484–485	−1.70	15			−11	4	0.54
H_b	15.39–15.43	499–500	1.15	17	37.79	1.99	no relationship		
	15.43–15.47	500–501	0.63	17			−19	5	0.53
	15.47–15.50	501–502	1.05	17			−13	6	0.27
H_a	16.79–16.81	544–545	–	7	37.84	2.04	no relationship		
	16.81–16.82	545–546	−0.95	20					
	16.82–16.83	546–547	−1.12	35					
	16.83–16.84	547–548	–	15					
	16.84–16.86	548–549	–	16					
ED	17.34–17.36	581–582	0.59	13	37.87	2.07	no relationship		
	17.36–17.38	582–583	0.90	17					
	17.38–17.43	583–584	−0.13	18					

*$\delta^{18}O_{sw}$ values from *G. ruber* (white) were collected from the same core intervals (Williams et al., 2012).

VSMOW. These results fall within the range of modern sea surface temperatures (Spear et al., 2011) and $\delta^{18}O_{sw}$ for the Gulf of Mexico (Watanabe et al., 2001) across an annual cycle. In three adjacent core intervals during the YD time slice (12.17–12.13 ka), $\delta^{18}O_c$ values range between −1.44 and 0.75‰ and Mg/Ca ratios from 2.6 to 7.7 mmol mol^{-1}. The lower Mg/Ca ratios correspond to a range of cooler sea surface temperatures during the YD (11.6–22.9°C).

The range of $\delta^{18}O_c$ values measured in multiple specimens from a single core interval varies across the entire deglaciation. During the deglaciation, the ice volume effect on $\delta^{18}O_{sw}$ is continuously changing, so we only compare ranges of measured $\delta^{18}O_c$. In the oldest time slices sampled (ED, H_a, and one core interval in H_b; Fig. 2), 96% of measured $\delta^{18}O_c$ values within each core interval fall within a tight range of 2.2‰. In contrast, the largest range of $\delta^{18}O_c$ for individual specimens from the sampled core intervals occurs during Heinrich Stadial 1 and the Bølling-Allerød, where time slices H_b, H_c, B_a, B_b, B_c, and B_d exhibit ranges of $\delta^{18}O_c$ values from 2.4‰ to 4.7‰ (Fig. 2a). The most negative $\delta^{18}O_c$ values among all individual shells appear during time slices B_b (−4.3‰ VPDB) and B_d (−4.4‰ VPDB); these time slices bracket MWP-1a, a <300 year period centered around ~14.6 ka (Deschamps et al., 2012).

Measured Mg/Ca ratios for all specimens deposited during Termination I range from 2.3 to 11.7 mmol mol^{-1} (10.4–27.3 °C) across the time intervals from the early deglaciation (ED; ~17.4 ka) through Bølling-Allerød time slice B_d (~13.4 ka), with mean Mg/Ca for each core interval ranging between ~4.5 and 6.1 mmol mol^{-1} (17.4–20.5 °C; Fig. 2b). Earlier in the record during time slices ED, H_a, and H_b (~17.4 to ~15.4 ka), the range of calculated $\delta^{18}O_{sw}$ for individual specimens spans ~2.0–3.2‰ (VSMOW), with 90% of values falling within a 2.2‰ range for each core interval. These ranges are comparable to the total range of $\delta^{18}O_{sw}$ values observed for the Holocene interval (~2‰ spread). Late Heinrich Stadial 1 time slice H_c (~15.0 ka) and Bølling-Allerød warm period time slices B_a, B_b, B_c, and B_d (~14.6 through ~13.4 ka) exhibit much greater variability among individual specimens, with reconstructed $\delta^{18}O_{sw}$ ranges ≥2‰ (Fig. 2c). The largest range of $\delta^{18}O_{sw}$ values (~5.3‰ spread) is observed within core intervals in time slice B_d (15.02–14.97 ka), which reflects the widest range of hydrographic conditions in the Gulf of Mexico over the Orca Basin.

3.2. Ba/Ca and salinity

Measured Ba/Ca_{shell} ratios from individual Holocene *O. universa* span a very tight range (0.6–1.3 μmol mol^{-1}; mean = 0.9 ± 0.2 μmol mol^{-1}; Fig. 3), which corresponds to reconstructed Ba/Ca_{sw} of 4.0–8.7 μmol mol^{-1} (eq. (3)). These seawater composition estimates are similar to measured Ba/Ca_{sw} ratios of 4.4 μmol mol^{-1} in the western Atlantic, near the Bahamas (Lea and Spero, 1994). Core intervals from the YD time slice (~12.15 ka) also have very tight ranges of measured Ba/Ca_{shell} ratios (0.6–1.5 μmol mol^{-1}; mean = 0.9 ± 0.1) that are comparable to Ba/Ca_{shell} observed in Holocene specimens (no significant difference; $p > 0.05$ for each YD core interval). When we apply eq. (4) to convert Ba/Ca_{shell} to salinity, these ratios yield salinities between 34.4 and 35.4 psu (Holocene) and 34.0 to 35.4 psu (YD). However, salinity variation at the modern core site is controlled by precipitation/evaporation, and not influenced by Mississippi River outflow. As a result, Holocene changes in [Ba] do not track changes in salinity, and Ba/Ca_{shell} of these samples is simply a recorder of Ba/Ca_{sw}.

The range of Ba/Ca among individual shells from the same core interval represents a range of salinity conditions during a short depositional interval. For deglacial-age specimens (~17.4 through ~13.4 ka) from all time slices except the YD and Holocene, 89% of core intervals exhibit ranges in Ba/Ca_{shell} >1.3 μmol mol^{-1} (Fig. 3). In these time slices, the mean Ba/Ca ratios among individual *O. universa* from single core intervals varies from 1.8 to 2.3 μmol mol^{-1}, which is 2–2.5x higher than for Holocene and YD specimens. These measured Ba/Ca ratios correspond to reconstructed salinities of 30.9–35.6 psu, which fall within the observed salinity tolerance for modern *O. universa* (Bijma et al., 1990). The highest measured Ba/Ca ratios (mean = 2.5 ± 0.9 μmol mol^{-1}; individual shells up to 4.8 μmol mol^{-1}) and the broadest range of Ba/Ca among specimens (range of 3.0–3.6 μmol mol^{-1}) occur in time slice H_c (15.03–14.97 ka), corresponding to a more pronounced effect of freshwater runoff in the core site vicinity. In individual ED (~17.4 ka) and H_a (~16.8 ka) specimens, 88% of measured Ba/Ca ratios are within a 1.4 μmol mol^{-1} range, and 91% are within a 1.5 μmol mol^{-1} range, respectively (Fig. 4), implying a narrow salinity range. However, mean Ba/Ca_{shell} ratios for deglacial time slices ED and H_a (2.1 ± 0.6 μmol mol^{-1} and 1.9 ± 0.6 μmol mol^{-1} respectively) are significantly higher ($p < 0.05$ for a *t*-test of each core interval) than mean Ba/Ca ratios in Holocene specimens (0.9 ± 0.2 μmol mol^{-1}; Figs. 3 and 4b), suggesting enhanced riverine influence on *O. universa* shell Ba/Ca early in the deglaciation.

Fig. 4a shows Mg/Ca vs. Ba/Ca for all *O. universa* specimens. Holocene specimens exhibit a broad Mg/Ca range (2.9–11.1 mmol mol^{-1}) but have a comparatively narrow Ba/Ca range (0.6–1.3 μmol mol^{-1}). YD specimens display a range of Ba/Ca ratios (0.6–1.5 μmol mol^{-1}) that is comparable to Holocene specimens, but have a narrower Mg/Ca range (2.6–7.7 mmol mol^{-1}) that is indicative of both lower maximum temperatures and a reduced annual temperature range. In contrast, the majority of deglacial intervals (ED through B_d; ~17.4 through ~13.4 ka) exhibit a broad range of Ba/Ca (0.6–4.8 μmol mol^{-1}), with Mg/Ca ratios ranging from 2.3 to 11.7 mmol mol^{-1} (10.4–27.3 °C). Mg/Ca and Ba/Ca ratios do not display covariation in any single time slice, suggesting that diagenetic overprinting is not likely to be a dominant process in the specimens we analyzed. The individual *O. universa* that were removed from the dataset during data reduction and quality control tend to have higher Ba/Ca ratios, but display Mg/Ca ratios in a range that is typical for *O. universa* (Fig. S-3).

3.3. $\delta^{18}O_w$ geochemistry through time

Reconstructed $\delta^{18}O_{sw}$ and salinity do not exhibit a constant relationship through time (Figs. 4b and 5). Data from Holocene and YD specimens cluster tightly and do not display a resolvable covariation between measured Ba/Ca and $\delta^{18}O_{sw}$ estimates (Fig. 5a; Fig. S-5). Among specimens from the early deglacial and Heinrich Stadial time slices ED and H_a, $\delta^{18}O_{sw}$ and salinity also do not covary, although the specimens prior to 15.5 ka do exhibit a broader range of $\delta^{18}O_{sw}$ values (Fig. 4b) than Holocene or YD specimens. The strongest covariation between $\delta^{18}O_{sw}$ and salinity occurs in data sets from core intervals in late Heinrich Stadial and Bølling-Allerød time slices H_b, H_c, B_a, B_b, B_c, and B_d, (Fig. 5b–5e; Figs. S-6–S-10). These intervals encompass the period of most rapid sea-level rise through the last deglaciation (Carlson and Clark, 2012). The linear relationships in each of the core intervals from 15.5 to 13.4 ka display clear mixing between open-ocean Gulf of Mexico seawater and LIS meltwater.

For the earliest time slices in the deglaciation (ED (~17.4 ka) and H_a (~16.8 ka)), measured Ba/Ca ratios are significantly higher than Holocene specimens ($p < 0.05$ for each core interval). Estimated salinities for these intervals are 31.9–35.2 psu (Fig. 4b), suggesting that *O. universa* calcified in a reduced-salinity environment that resulted from mixing of Mississippi River water into the photic zone over the Orca Basin. Despite evidence of reduced surface

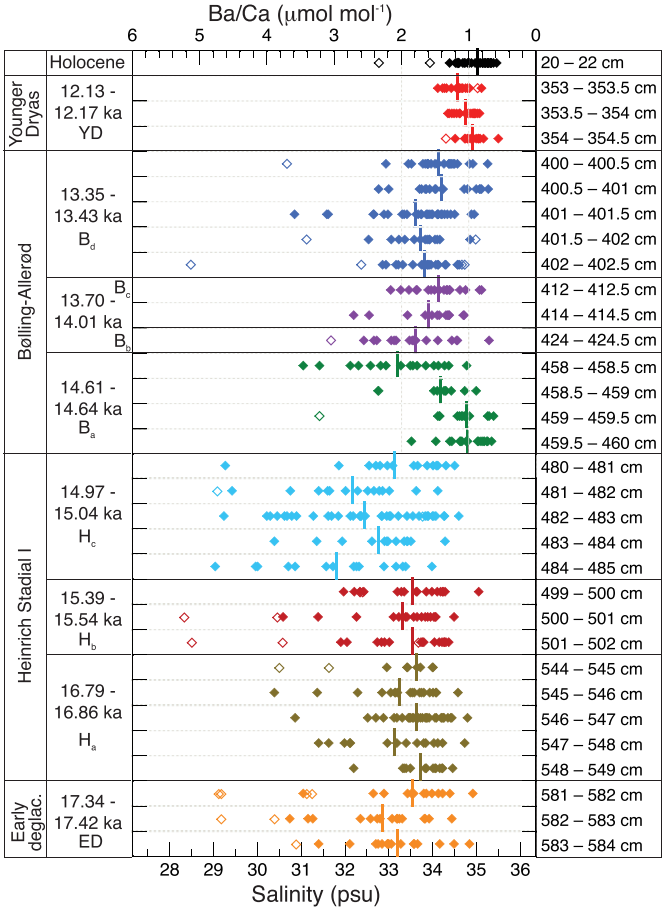

Fig. 3. Measured Ba/Ca (μmol mol^{-1}) for all individual *O. universa* specimens, measured by LA-ICP-MS depth profiling. Time slice designations follow the same designations as Fig. 2. Open symbols indicate data points that were excluded during LA-ICP-MS data analysis and quality control, as in Fig. 2b. Salinity on the x-axis is calculated using eq. (4).

salinity in time slice H_a, reconstructed $\delta^{18}O_{sw}$ does not covary with Ba-derived salinity in time slices ED (~17.4 ka) and H_a (~16.8 ka) (Fig. 5f; Figs. S-11 and S-12).

During late Heinrich Stadial 1 and the Bølling-Allerød, 20 core intervals were analyzed with 0.5–1 cm resolution (15–30 year time slices) between 15.5 and 13.4 ka (time slices H_b, H_c, B_a, B_b, B_c, and B_d). For each interval, we calculate a linear regression between $\delta^{18}O_{sw}$ and S. The y-intercept quantifies the $\delta^{18}O_w$ of Mississippi River discharge, which was dominantly controlled by LIS meltwater (Licciardi et al., 1999; Teller, 1990a, b; Wickert, 2016), rather than local or regional precipitation (Fig. 5b–e; all regressions are shown in Supplemental Figs. S-4 through S-11). LIS meltwater $\delta^{18}O_w$ values, calculated using a York linear regression method, vary between −11(±4)‰ to −38(±8)‰ VSMOW (Table 2). The more enriched $\delta^{18}O_w$ values calculated for a meltwater endmember occur earlier in the record (~15.5 ka), within the earliest time slices that display linear covariation between $\delta^{18}O_{sw}$ and salinity that is sufficient to allow a meaningful linear regression. The most negative $\delta^{18}O_w$ endmember estimates occur during time slices B_b, B_c, and B_d (~14.0 through 13.3 ka), near the peak influx of LIS meltwater into the Gulf of Mexico (after Williams et al., 2012, Fig. 6b and c).

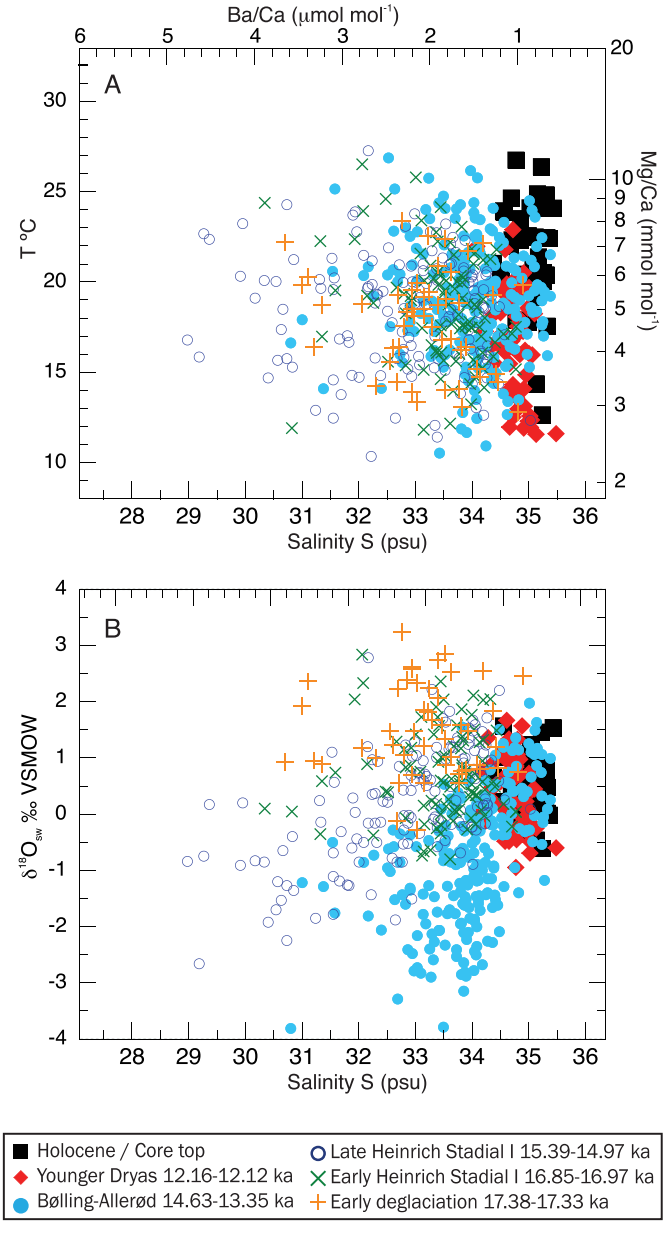

Fig. 4. A) Ba/Ca vs. Mg/Ca ratios from LA-ICP-MS analyses with computed salinities and temperatures. **B)** Salinity vs. calculated $\delta^{18}O_{sw}$ for individual *O. universa* from all intervals.

4. Discussion

4.1. Geochemistry of a freshwater endmember

Early studies of LIS meltwater in the Gulf of Mexico identified several episodes of anomalously negative $\delta^{18}O_c$ values between ~18 and 11 ka that were consistent with a depleted meltwater signal (Kennett and Shackleton, 1975; Leventer et al., 1982) and characteristic low-salinity foraminiferal assemblages during the deglaciation (Kennett et al., 1985). Other records with more precise age control have demonstrated variations in the volume of LIS meltwater delivered to the Gulf of Mexico (Flower et al., 2004), with rapid and high frequency shifts in surface water $\delta^{18}O_{sw}$ on decadal timescales (Williams et al., 2012). All support the variable influence of LIS meltwater in the Gulf of Mexico during the last deglaciation (Flower et al., 2011). In addition to an isotopic signature from LIS meltwater, evidence from proxies of continental erosion (Brown and Kennett, 1998; Marchitto and Wei, 1995; Meckler et al., 2008) indicates that a large volume of freshwater runoff from the LIS was directed into the Gulf of Mexico during the last deglaciation, with a dynamic melting history and periods of high meltwater discharge (Brown and Kennett, 1998).

Table 2 shows freshwater oxygen isotope values and 1-sigma confidence intervals for each $\delta^{18}O_{sw}$-salinity regression, using $\delta^{18}O_{sw}$ and S values with propagated errors from analytical measurements and proxy conversion equations, and an estimate of open-ocean geochemistry. The confidence intervals on the calculated y-intercepts range from ±3‰ to ±10‰ (Table 2). This uncertainty is partially due to a physiological limitation on the salinity tolerances of planktic foraminifers, as individual $\delta^{18}O_{sw}$ -S pairs are limited to a ~5 psu range of open-ocean salinity recorded in *O. universa* shells. While a larger salinity range would both improve the confidence intervals on the y-intercept and better constrain our estimates of the $\delta^{18}O_w$ value of LIS meltwater, ultimately the precision of the regression technique is limited by the physiological constraint that *O. universa* does not calcify at salinities <27 psu (Bijma et al., 1990).

In order to estimate the $\delta^{18}O_{sw}$ and S of the open-ocean, several sources of uncertainty in deglacial Gulf of Mexico geochemistry must be considered. Unrelated to ice volume and meltwater contributions, the background salinity in the Gulf of Mexico likely varied during the LGM and throughout the deglaciation. Today, surface waters in the Gulf of Mexico are supplied from the western Caribbean via the Yucatan Current and the Loop Current. During Heinrich Stadial 1 and the Younger Dryas, changes in Atlantic Meridional Overturning Circulation caused an increase in $\delta^{18}O_{sw}$ values that propagated into the subtropical Atlantic and the Caribbean (Carlson et al., 2008b), which would have affected $\delta^{18}O_{sw}$ values in the Gulf of Mexico. Additionally, precipitation in the Caribbean and Gulf of Mexico may have been affected by the migration of the intertropical convergence zone (Schmidt et al., 2006), and records from the Florida Straits show progressive enhancement of precipitation during Termination I, with an abrupt salinity increase at the Younger Dryas (Schmidt and Lynch-Stieglitz, 2011). Further evidence suggests variations in freshwater input on glacial/interglacial timescales to the Caribbean, sourced from the Magdalena River and its catchment area that extends into tropical South America (Mora and Martínez, 2005).

Constraining the relationship between [Ba] and salinity in the

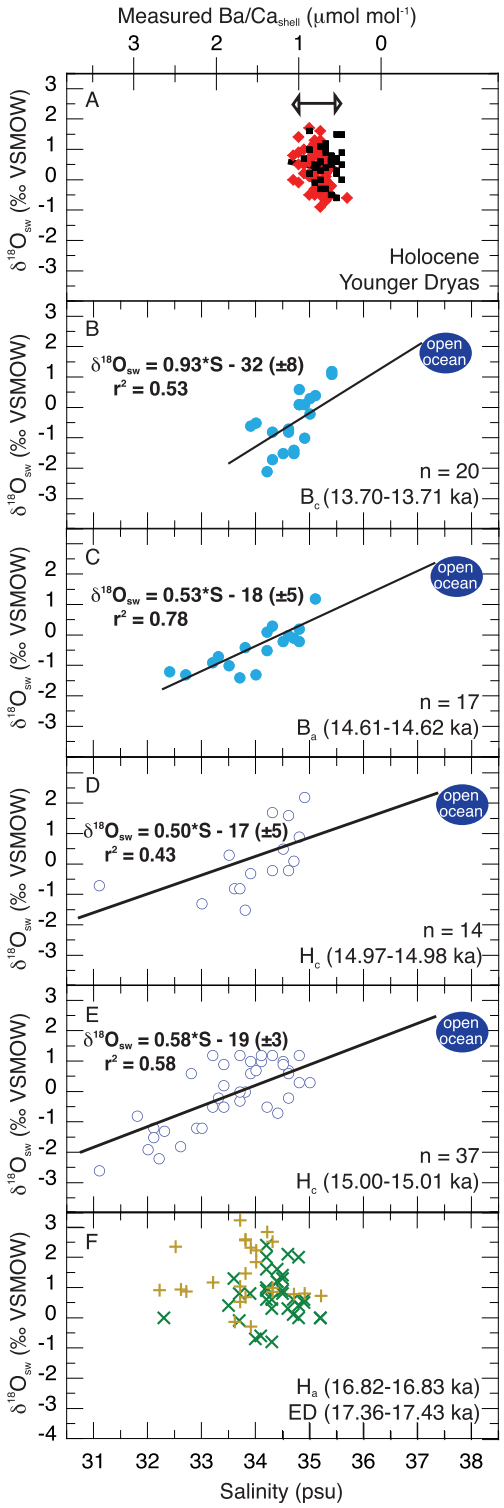

Fig. 5. Calculated $\delta^{18}O_{sw}$ values and Ba-derived salinity estimates for individual *O. universa* from selected core intervals. **A)** In Holocene (black squares) and Younger Dryas (YD; red diamonds) specimens, Ba/Ca_{shell} does not record salinity variation from fluvial input, and no relationship is observed between $\delta^{18}O_{sw}$ and Ba/Ca_{shell}. Double-headed arrow shows predicted Ba/Ca_{shell} ratios, based on measured Ba/Ca_{sw} in the Gulf of Mexico and the Ba/Ca_{shell}-Ba/Ca_{sw} conversion from Hönisch et al. (2011). **B—E)** During the deglaciation, linear regressions of individual core intervals yield $\delta^{18}O_w$ values of LIS meltwater. The open-ocean end-member values (blue circles) evolve through the deglaciation (see text for details). York regression statistics are shown for each dataset, calculated with the open-ocean end-member included. We present examples from Bølling-Allerød time slices B_c and B_a **(B, C)** and Heinrich Stadial 1 time slice H_c **(D, E)**. **F)** Specimens from time slices early in the deglaciation (H_a, ED) show elevated [Ba] with respect to Holocene and Younger Dryas specimens, suggesting the influence of continental runoff, but we do not observe a correlation between $\delta^{18}O_{sw}$ and salinity. (For interpretation of the references to colour in this figure legend, the reader is referred to the web version of this article.)

Gulf of Mexico in the past also presents challenges. The Ba-salinity conversion we use is based on measurements of modern freshwater outflow from the Mississippi-Atchafalaya River, with water samples collected at high, middle, and low river stages (Hanor and Chan, 1977; Joung and Shiller, 2014) over 3 different years (Fig. S-2). The maximum open-ocean endmember of this mixing relationship is constrained by the maximum measured salinity from the modern data set (35 psu; Hanor and Chan, 1977; Joung and Shiller, 2014). During the LGM, open-ocean salinity increased 1–2 psu, which would cause the regression slope to change (dependent on each dataset; Figs. S-6 through S-10) and affect the y-intercept. The modern relationship between trace metal concentration and discharge in the Mississippi River also has a slight dependence on the proportion of water from the Ohio and Missouri River tributaries (Shiller, 1997; Shiller and Boyle, 1987). However, while the geographic extent and underlying bedrock of the Mississippi River watershed was constantly changing during Termination I, the Mississippi River drainage included the geographic extent of the modern watershed until the YD (Licciardi et al., 1999; Wickert, 2016). Monthly trace element time-series measurements from the Lower Mississippi River also demonstrate that seasonal variations in [Ba] from the watershed are relatively invariant (Shiller, 1997).

4.2. Reconstructing $\delta^{18}O_{sw}$ and paleosalinity

In the modern Gulf of Mexico, precipitation is depleted in ^{18}O relative to ocean water via Rayleigh fractionation, and $\delta^{18}O_{sw}$ and S covary because both parameters are governed by the balance between evaporation and precipitation. Unlike the $\delta^{18}O$ of fluvial freshwater, the $\delta^{18}O$ of precipitation over the open ocean is very close to VSMOW, so the slope of the $\delta^{18}O_{sw}$-S relationship can be as small as 0.1‰ psu^{-1} (Fairbanks et al., 1992). As a result, it is unlikely that a salinity change of 4 psu preserved in a sediment assemblage would record changes in salinity solely due to changes in precipitation, but instead due to freshwater input from a fluvial source.

During the Holocene and YD, we do not observe a trend between $\delta^{18}O_{sw}$ and Ba/Ca in our data (Fig. 4b). Broecker et al. (1989) proposed a significant reduction in flow down the Mississippi River during the YD to explain this lack of a meltwater signal in Orca Basin sediment core records. Although a redirection of meltwater flow away from the Gulf of Mexico could explain these data, we note that the Orca Basin is located 300 km southwest of the modern Mississippi River Delta, and modern salinity over the Orca Basin is insensitive to riverine outflow. By ~13.0 ka, sea level had risen by ~60–70 m (Carlson and Clark, 2012; Clark et al., 2009), so the paleoshoreline during the YD had receded northward by > 50 km and the Orca Basin was no longer proximal to the mouth of the Mississippi River. As a result, during the YD and into the Holocene, the Ba/Ca_{shell} ratios recorded in shell calcite may not have reflected changes in salinity related to continental runoff. Instead, Ba/Ca_{shell} in YD and Holocene intervals likely records a range of open-ocean Ba/Ca_{sw} ratios that are consistent with independently reported regional Ba/Ca_{sw} (Fig. 5a; Lea and Spero, 1994).

Paleoceanographic interpretations of $\delta^{18}O_c$ data from deep-sea cores generally rely on the assumption that $\delta^{18}O_c$ variations result from changes in either temperature or $\delta^{18}O_{sw}$, depending on the depositional setting. Previous studies have combined $\delta^{18}O_c$ measurements with faunal assemblages (Cortijo et al., 1994, 1999) and bulk Mg/Ca ratios of foraminifera (Irvalı et al., 2012; Winsor et al., 2012) to infer that the dominant control on foraminiferal $\delta^{18}O_c$

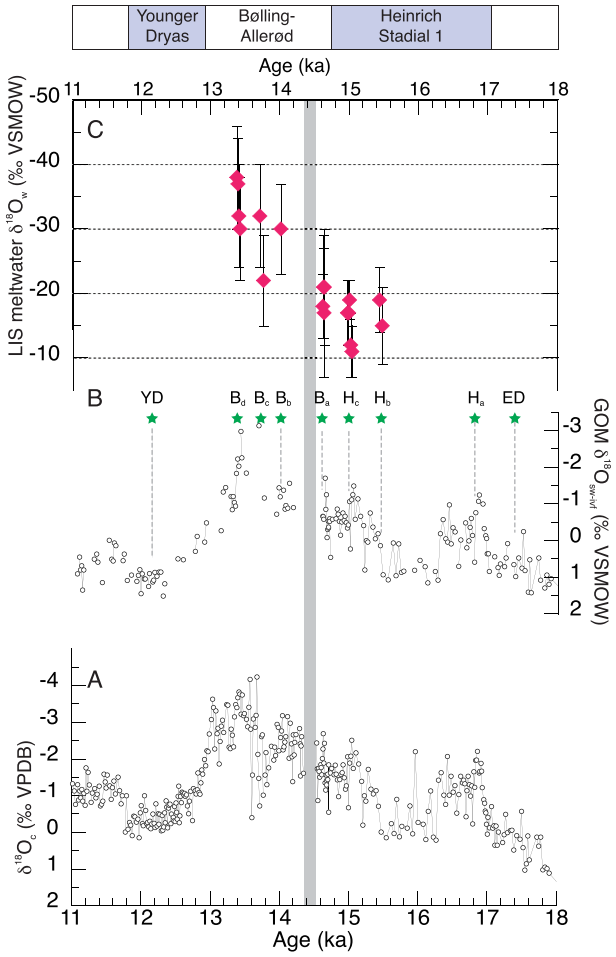

Fig. 6. A) $\delta^{18}O_c$ from multiple shell *G. ruber* (white) samples from MD02-2550 (data from Williams et al., 2012). **B)** Computed $\delta^{18}O_{sw}$ record from Mg/Ca and $\delta^{18}O_c$ analyses of *G. ruber* (white) from MD02-2550 (ice volume corrected), after Williams et al. (2012). Core intervals (time slices) from MD02-2550 used in this study are indicated by green stars. **C)** Estimated $\delta^{18}O_w$ values of LIS meltwater entering the Gulf of Mexico during Termination I, from 0.5 to 1 cm thick core intervals. The $\delta^{18}O_w$ values of the freshwater end-member are calculated using a York linear regression on linked $\delta^{18}O_{sw}$-salinity data from individual *O. universa*, using an open-ocean end-member estimate as an additional unweighted data point in the regression. Estimated $\delta^{18}O_w$ values are shown for significant relationships only, with 1-sigma confidence intervals around the y-intercepts (Table 2). Vertical grey bar indicates ~10 cm interval in MD02-2550 where no foraminifera are present. (For interpretation of the references to colour in this figure legend, the reader is referred to the web version of this article.)

(temperature or $\delta^{18}O_{sw}$) may switch back and forth between core intervals in a single location. Here we approach the same question using $\delta^{18}O_c$ and Mg/Ca (T), with both parameters measured in individual shells (Fig. 7a). Our data for Holocene and YD specimens show that these two parameters are strongly correlated ($r^2 = 0.48$, $n = 95$), whereas in the other intervals in our Orca Basin study $\delta^{18}O_c$ and Mg/Ca data are nearly randomly distributed. The changes in temperature (~21 °C) and $\delta^{18}O_c$ (~3.0‰) yield a slope of 0.26‰ °C^{-1}, which is very close to the fractionation for calcite relative to temperature in paleotemperature equations. These data demonstrate that temperature is the primary control on foraminiferal $\delta^{18}O_c$ during the YD and Holocene.

The impact of $\delta^{18}O_{sw}$ on shell $\delta^{18}O_c$ values during Termination I can be clearly seen in Fig. 7b. Here, the range in $\delta^{18}O_{sw}$ (~7.5‰ VSMOW) and $\delta^{18}O_c$ (~6.5‰ VPDB) are nearly identical, as would be expected if shell $\delta^{18}O_c$ is governed primarily by $\delta^{18}O_{sw}$. The covariation between $\delta^{18}O_{sw}$ and $\delta^{18}O_c$ for all deglacial specimens prior to the YD displays a slope of 0.88 ($r^2 = 0.76$). These data demonstrate that during Termination I, $\delta^{18}O_c$ variability among individual foraminifers is predominantly controlled by variations in $\delta^{18}O_{sw}$. It is possible that similar comparisons, using multiple measurements on single foraminifera, could be applied in other depositional settings to deconvolve changes in precipitation/salinity from a temperature signal in deep-sea core data sets.

Interestingly, in the earliest time slices we analyzed from 17.4 to 16.8 ka (ED and H_a time slices), we do not see a clear relationship between Ba-derived salinity and $\delta^{18}O_{sw}$ for individual *O. universa* specimens, and $\delta^{18}O_{sw}$ vs. S data do not yield statistically meaningful regression intercepts for $\delta^{18}O_w$ (Fig. 5f; Figs. S-11 and S-12). Although the range of Ba/Ca is narrow in these datasets (<1.5 μmol mol^{-1}), mean Ba/Ca ratios are elevated, suggesting that Mississippi River freshwater did influence the surface waters above the Orca Basin earlier in the deglaciation 17.4–16.8 ka. If the isotopic composition of continentally-derived freshwater during this time was controlled by precipitation, we would not be able to constrain the slope or y intercepts as they would be near zero.

In the Orca Basin, downcore changes in measured Ba/Ca unequivocally reflect Mississippi River freshwater influence. However, reconstructing the $\delta^{18}O_w$ value of freshwater end-member is ultimately dependent on mixing of open-ocean $\delta^{18}O_{sw}$ with a single source for variations in both $\delta^{18}O_w$ and [Ba]. Early in the deglaciation, the Mississippi River drainage basin was likely a mixture of regional precipitation with LIS meltwater. This mixture was either dominated by precipitation or included meltwater with an isotopic composition that did not differ substantially from precipitation. Because the Orca Basin was closer to the deglacial Gulf of Mexico paleoshoreline, it is likely that we would still observe a significant surface freshwater contribution with elevated Ba as a function of increased river input, although $\delta^{18}O_{sw}$ values would not reflect an LIS source. Together, our early deglaciation (~17.4–15.5 ka) data suggest that the routing of LIS meltwater into the Gulf of Mexico was not constant across Termination I, which agrees with earlier interpretations of sedimentary records (Flower et al., 2011). However, our data cannot confirm the presence of an isotopically distinct LIS meltwater in the Gulf of Mexico at ~17 ka, as suggested from records based on *Globigerinoides ruber* (Wickert et al., 2013; Williams et al., 2012).

The peak meltwater influence in the Gulf of Mexico occurred during latest Heinrich Stadial 1 and through the Bølling-Allerød (Williams et al., 2012), which occurred during the 11–18 m sea level rise of MWP-1a (centered on 14.6 ka; Deschamps et al., 2012). In this Orca Basin core, MWP-1a is expressed as a 24 cm thick interval with no planktic foraminifera (431–455 cm; 14.66–14.11 ka), likely resulting from surface salinity in the Gulf of Mexico that decreased below the tolerance for living foraminifera. For the time slices in our dataset that bracket MWP-1a (H_c, B_a, B_b, B_c, and B_d; spanning 15.4 to 13.5 ka), estimated $\delta^{18}O_{sw}$ values from individual *O. universa* range from −4.45 to +1.44‰ VSMOW (Fig. 6d), which is consistent with a >4‰ spread between individual *O. universa* $\delta^{18}O_c$ measured in nearby Orca Basin core EN32-PC6 (Spero and Williams, 1990). The lowest salinities recorded by individual shells occur at ~15.0 ka during time slice H_c (Fig. 3). However, the most negative $\delta^{18}O_{sw}$ values do not occur until ~13.4 ka, in time slice B_d during the Bølling-Allerød (Fig. 2c). Together, these results demonstrate that LIS meltwater was isotopically heterogeneous during peak meltwater influence in the Gulf of Mexico from 15.5 to 13.3 ka (time slices H_b through B_d), with a $\delta^{18}O_w$ range between −11‰ and −38‰ (Fig. 6c; Table 2). These results encompass a range of $\delta^{18}O_w$ values that are consistent with model estimates for the oxygen isotope geochemistry of different sections of the LIS (e.g., Ferguson and Jasechko, 2015; Schwarcz and Eyles, 1991; Sima et al., 2006).

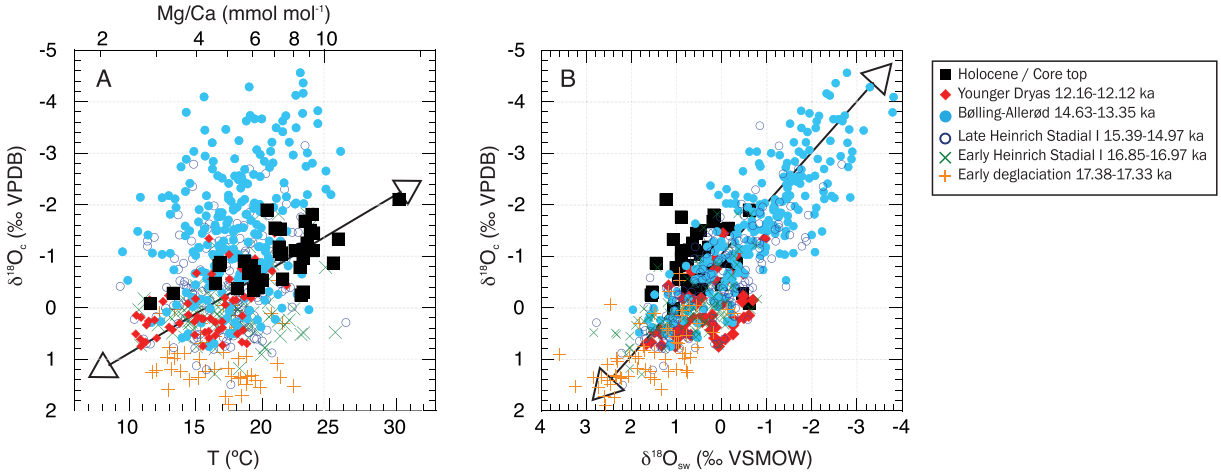

Fig. 7. A) Measured shell $\delta^{18}O_c$ vs. temperature (converted from measured Mg/Ca) for all *O. universa* specimens. Note that Mg/Ca data from the Holocene and Younger Dryas intervals vary with $\delta^{18}O_c$, whereas shells from deglacial intervals show little relationship to temperature. Double-headed arrow shows linear trend of the temperature dependence of $\delta^{18}O_c$ for combined Holocene and Younger Dryas specimens only (red and black points only; $\delta^{18}O_c = -0.26*T(°C) + 4.58$; $r^2 = 0.48$). This is close to the slope we expect due to the relative insensitivity of the Orca Basin to freshwater perturbations during these time intervals. **B)** Measured shell $\delta^{18}O_c$ vs. calculated $\delta^{18}O_{sw}$ for all *O. universa* specimens. Here, salinity ($\delta^{18}O_{sw}$) is the dominant control on shell $\delta^{18}O_c$ during the deglacial time slices but displays no covariation in Younger Dryas or Holocene intervals. Double-headed arrow shows linear trend for all combined deglacial specimens (all points except YD (red) and Holocene (black); $\delta^{18}O_c = 0.88*\delta^{18}O_{sw} - 0.72$; $r^2 = 0.76$), indicating that $\delta^{18}O_c$ is strongly controlled by $\delta^{18}O_{sw}$ during the deglaciation. (For interpretation of the references to colour in this figure legend, the reader is referred to the web version of this article.)

Previous studies have assumed a single $\delta^{18}O$ estimate when calculating meltwater input (−25 or −35‰; Aharon, 2006; Carlson, 2009; Carlson et al., 2007; Hill et al., 2006; Obbink et al., 2010; Wickert et al., 2013). The heterogeneity in LIS meltwater $\delta^{18}O$ shown in our results suggests that this may be a simplistic approach, especially when estimating the volumetric contributions to sea-level rise during different time intervals. For time slices from 15.5 through 14.6 ka in our data, $\delta^{18}O_w$ value estimates near −17‰ indicates that early deglacial discharge estimates based on isotopic constraints may underestimate the amount of melting (Wickert et al., 2013). Conversely, meltwater volume from the LIS during the Bølling and Allerød may be overestimated (Aharon, 2006; Carlson, 2009; Wickert et al., 2013), if $\delta^{18}O_w$ values as negative as −38‰ were the dominant isotopic signal in the Mississippi River watershed.

4.3. LIS melting history

Modern continental ice sheets exhibit considerable $\delta^{18}O_{ice}$ heterogeneity, which varies in response to altitude, latitude, the adiabatic lapse rate, and the temperature of the ice surface when snow falls (Masson-Delmotte et al., 2008, and references therein). Isotope-enabled GCMs have been used to simulate the geographic distribution of oxygen isotope values in precipitation (Carlson et al., 2008a; LeGrande et al., 2006; Pausata et al., 2011; Risi et al., 2010; Ullman et al., 2014; Werner et al., 2011; Yoshimura et al., 2008). Paleohydrologic records and modeling studies of North America from the LGM show that westerly storm tracks were shifted southward and intensified during the LGM (Oster et al., 2015, and references therein), and $\delta^{18}O$ records also indicate that precipitation was up to 7‰ more negative during glacial intervals (Jasechko et al., 2015). Variation in Greenland $\delta^{18}O$ values has also been attributed to southward shifts in storm tracks and moisture sources (Seierstad et al., 2014). Simple isotopic models of the LIS incorporate latitude, altitude, and temperature variation, and these models predict minimum LIS $\delta^{18}O_w$ values of −30 to −35‰ for the top of a ~3 km-high ice sheet (Sima et al., 2006). However, these do not incorporate parameters that affect the isotopic composition of rainfall today, such as relative humidity, adiabatic lapse rate, and Rayleigh fractionation within clouds due to successive rainout events (Bowen and Wilkinson, 2002). Although atmospheric parameters such as relative humidity are important determinants of the oxygen isotopic value of precipitation, they are difficult to constrain in the past (Hoffmann et al., 1998; Risi et al., 2010).

Several studies have estimated the $\delta^{18}O_w$ of LIS meltwater indirectly from lacustrine sediment records from proglacial lakes near the southern margin of the LIS. Measurements of lacustrine calcite concretions suggest that $\delta^{18}O_w$ ranged from −30‰ to −32‰ for basal ice and −16‰ to −19‰ for southern margin melt (Hillaire-Marcel and Causse, 1989; Hillaire-Marcel et al., 1979). Ostracode records from a proglacial lacustrine sequence in the St. Lawrence drainage (eastern Canada) estimate that lakewater $\delta^{18}O_w$ ranged from −12‰ to −21‰, suggesting either more positive LIS $\delta^{18}O_w$ values or mixing with non-glacial sources (Eyles and Schwarcz, 1991; Hladyniuk and Longstaffe, 2016). The effect of surface evaporation on the isotopic value and stratification of supraglacial lakes and long-lived proglacial lakes, such as Lake Agassiz, could have also influenced these values over the course of full LIS melting (Buhay and Betcher, 1998). Most of these records are Holocene in age and postdate the primary melting phase of the LIS during Termination I. As a result, these are likely to yield estimates of LIS $\delta^{18}O$ that are more positive than LGM values, following the climate signal that is seen in Greenland when comparing Holocene ice (−26 to −36‰; Vinther et al., 2009) to LGM ice (−40 to −45‰; Buizert et al., 2014; Johnsen et al., 1972; Seierstad et al., 2014). The most direct measurements of LIS remnants, from ice on the Barnes Ice Cap, yield $\delta^{18}O$ values of −21 to −40‰ (Hooke and Clausen, 1982) at a high-latitude site (70°N) on Baffin Island proximal to a marine isotopic source (Andrews et al., 2002). Given the $\delta^{18}O$ values of LGM ice on Greenland, and LIS model estimates with maximum thickness of 3–4 km (Argus et al., 2014; Gregoire et al., 2012; Peltier et al., 2015), it is not unreasonable to expect more negative isotopic values as well as greater heterogeneity in meltwater derived from the central LIS. Regional temperatures in the interior of North America up to 25°C colder than modern values (Annan and Hargreaves, 2013) would also have contributed to extremely

negative precipitation $\delta^{18}O$ values over the LIS.

In our record, core intervals prior to MWP-1a (15.5–14.6 ka; time slices H_b, H_c, and B_a in Fig. 6c) display LIS meltwater $\delta^{18}O_w$ values that vary between -11 ± 4‰ and -21 ± 9‰ (Table 2). These more ^{18}O-enriched isotopic values are consistent with independent calculations of the $\delta^{18}O$ of the LIS that yield more positive values (Ferguson and Jasechko, 2015), and are consistent with meltwater sources from lower-elevation, lower-latitude, warmer portions of the ice sheet. During the Bølling and Allerød (14.0–13.3 ka; time slices B_b, B_c, and B_d in Fig. 6c), LIS meltwater $\delta^{18}O_w$ values range between -22 ± 7‰ to -38 ± 8‰ (Table 2). These values fall within the range of oxygen isotope values observed in modern Antarctic precipitation (−18 to −55‰), although they are more positive than the more ^{18}O-depleted (−50 to −57‰) at 3–4 km elevation on the East Antarctic Ice Sheet (Ekaykin et al., 2002; Masson-Delmotte et al., 2008; Morgan, 1982; Stenni et al., 2001). During Termination I, LIS seasonally drained through the Mississippi River watershed (Kehew and Teller, 1994; Licciardi et al., 1999; Teller and Kehew, 1994), and the ^{18}O-depleted values from our study suggest that at times, Mississippi River outflow was dominated by meltwater from the high-latitude, high-elevation interior of the ice sheet. As Termination I melting progressed into the Bølling-Allerød, meltwater $\delta^{18}O_w$ value estimates become progressively negative, suggesting the potential for sequential mining of the interior of the LIS as it retreated. This progression towards more negative values suggests an increased proportion of ice that originated in the high-elevation LIS interior and subsequently flowed to the southern margin.

The range of $\delta^{18}O_w$ values we calculate is consistent with LIS meltwater being derived from multiple distinct sources on the North American continent. Isotope-based interpretations of varying LIS meltwater sources are supported by provenance records from the Gulf of Mexico that indicate changes in clay mineralogy, which reflects terrigenous input from different regions of the Mississippi River catchment (Montero-Serrano et al., 2009; Sionneau et al., 2010). Two distinct provinces emerge from these records: the illite- and chlorite-rich Ohio River valley, which was in the drainage path of the southern LIS, and the smectite-rich Missouri River catchment (western Mississippi River contribution), which received meltwater from the southwestern LIS (Wickert, 2016). The regression technique using foraminiferal geochemical data that we present in this paper opens the potential for a direct link between meltwater $\delta^{18}O$ geochemistry and the geographic origin of meltwater from within the ice sheet.

5. Conclusions

Geochemical analyses of populations of individual foraminifers from discrete core intervals provide the opportunity to extract an additional dimension of environmental and ecological information from the fossil record that is obscured by the traditional bulk analysis approach. Here we demonstrate that the breadth of environmental conditions recorded by the planktic foraminifer *O. universa* yield a more detailed reconstruction of water column hydrography during ice sheet meltwater events in the Gulf of Mexico. Our $\delta^{18}O_w$ records of LIS meltwater from the Orca Basin sediment in the Gulf of Mexico indicate a dynamic LIS melting history over the course of the last deglaciation. We present the first marine geochemical record that indicates variability in meltwater $\delta^{18}O_w$ values. Our results quantify $\delta^{18}O$ heterogeneity in individual LIS meltwater time periods, confirm sourcing of meltwater from different portions of the LIS with different $\delta^{18}O_{ice}$ values, and demonstrate that the $\delta^{18}O_w$ value of LIS meltwater varied on decadal timescales during the deglaciation.

Acknowledgements

This research was substantially influenced by conversations with Lauren Gregoire, Jennifer Fehrenbacher, and Heather Hill. We gratefully acknowledge the technical expertise of Graham Nash (ANU) and Dave Winter (UCD), and laboratory assistance from Lisa Jacobs and Eric Naumann (UCD Stable Isotope Laboratory). We thank two anonymous reviewers, whose comments and suggestions contributed to and improved a previous version of this manuscript. Portions of this project were partially funded by an ExxonMobil Student Research Grant (LV) and the Durrell Fund in the Department of Earth and Planetary Science, UC Davis (LV). This research was supported by National Science Foundation grants OCE-1061676 and EAR-0946297 (HJS).

During the research phase of this project, our dear friend, colleague, and mentor, Ben Flower, passed away. This project builds on Ben's passion to understand the linkage between deglacial climate history and the melting dynamics of the Laurentide Ice Sheet. We all miss Ben.

Appendix A. Supplementary data

Supplementary data related to this article can be found at https://doi.org/10.1016/j.quascirev.2017.10.007.

References

Adkins, J.F., McIntyre, K., Schrag, D.P., 2002. The salinity, temperature, and delta ^{18}O of the glacial deep ocean. Science 298, 1769–1773. https://doi.org/10.1126/science.1076252.

Aharon, P., 2003. Meltwater flooding events in the Gulf of Mexico revisited: implications for rapid climate changes during the last deglaciation. Paleoceanography 18, 1079. https://doi.org/10.1029/2002PA000840.

Aharon, P., 2006. Entrainment of meltwaters in hyperpycnal flows during deglaciation superfloods in the Gulf of Mexico. Earth Planet. Sci. Lett. 241, 260–270. https://doi.org/10.1016/j.epsl.2005.10.034.

Allison, M.A., Demas, C.R., Ebersole, B.A., Kleiss, B.A., Little, C.D., Meselhe, E.A., Powell, N.J., Pratt, T.C., Vosburg, B.M., 2012. A water and sediment budget for the lower Mississippi-Atchafalaya River in flood years 2008-2010: implications for sediment discharge to the oceans and coastal restoration in Louisiana. J. Hydrology 432–433, 84–97. https://doi.org/10.1016/j.jhydrol.2012.02.020.

Anand, P., Elderfield, H., Conte, M.H., 2003. Calibration of Mg/Ca thermometry in planktonic foraminifera from a sediment trap time series. Paleoceanography 18. https://doi.org/10.1029/2002kpa000846.

Andrews, J., Holdsworth, G., Jacobs, J., 2002. Glaciers of the Arctic Islands. Glaciers of Baffin Island. USGS Professional Paper 1386-J-1, pp. J165–J198.

Annan, J., Hargreaves, J., 2013. A new global reconstruction of temperature changes at the last glacial maximum. Clim. Past 9, 367–376. https://doi.org/10.5194/cp-9-367-2013.

Argus, D.F., Peltier, W., Drummond, R., Moore, A.W., 2014. The Antarctica component of postglacial rebound model ICE-6G_C (VM5a) based on GPS positioning, exposure age dating of ice thicknesses, and relative sea level histories. Geophys. J. Int. 198, 537–563. https://doi.org/10.1093/gji/ggu140.

Bé, A.W.H., 1977. An ecological, zoogeographic and taxonomic review of recent planktonic foraminifera. In: Ramsay, A.T.S. (Ed.), Oceanic Micropaleontology. Academic Press, London, pp. 1–100.

Bé, A.W.H., Harrison, S.M., Lott, L., 1973. *Orbulina universa* d'Orbigny in the indian ocean. Micropaleontology 19, 150–192.

Bemis, B.E., Spero, H.J., Bijma, J., Lea, D.W., 1998. Reevaluation of the oxygen isotopic composition of planktonic foraminifera: experimental results and revised paleotemperature equations. Paleoceanography 13, 150–160.

Bijma, J., Faber, W.W., Hemleben, C., 1990. Temperature and salinity limits for growth and survival of some planktonic foraminifera. J. Foraminifer. Res. 20, 95–116.

Billups, K., Spero, H.J., 1996. Reconstructing the stable isotope geochemistry and paleotemperatures of the equatorial Atlantic during the last 150,000 years: results from individual foraminifera. Paleoceanography 11, 217–238. https://doi.org/10.1029/95PA03773.

Birks, S.J., Edwards, T.W.D., Remenda, V.H., 2007. Isotopic evolution of Glacial Lake Agassiz: new insights from cellulose and porewater isotopic archives. Palaeogeogr. Palaeoclimatol. Palaeoecol. 246, 8–22. https://doi.org/10.1016/j.palaeo.2006.10.024.

Bowen, G.J., Wilkinson, B., 2002. Spatial distribution of delta O-18 in meteoric precipitation. Geology 30, 315–318. https://doi.org/10.1130/0091-7613(2002).

Boyle, E.A., 1976. The Marine Geochemistry of Trace Metals, Joint Program in Oceanography. Massachusetts Institute of Technology and Woods Hole

Oceanographic Institution, p. 156.
Broecker, W.S., Kennett, J.P., Flower, B.P., Teller, J.T., Trumbore, S., Bonani, G., Wolfli, W., 1989. Routing of meltwater from the Laurentide Ice Sheet during the Younger Dryas cold episode. Nature 341, 318–321. https://doi.org/10.1038/341318a0.
Brown, P.A., Kennett, J.P., 1998. Megaflood erosion and meltwater plumbing changes during last North American deglaciation recorded in Gulf of Mexico sediments. Geology 26, 599–602. https://doi.org/10.1130/0091-7613(1998)026<0599:meampc>2.3.co;2.
Buhay, W.M., Betcher, R.N., 1998. Paleohydrologic implications of O-18 enriched Lake Agassiz water. J. Paleolimnol. 19, 285–296. https://doi.org/10.1023/A:1007938200730.
Buizert, C., Gkinis, V., Severinghaus, J.P., He, F., Lecavalier, B.S., Kindler, P., Leuenberger, M., Carlson, A.E., Vinther, B., Masson-Delmotte, V., 2014. Greenland temperature response to climate forcing during the last deglaciation. Science 345, 1177–1180. https://doi.org/10.1126/science.1254961.
Carlson, A.E., 2009. Geochemical constraints on the Laurentide Ice Sheet contribution to Meltwater Pulse 1A. Quat. Sci. Rev. 28, 1625–1630. https://doi.org/10.1016/j.quascirev.2009.02.011.
Carlson, A.E., Clark, P.U., 2012. Ice sheet sources of sea level rise and freshwater discharge during the last deglaciation. Rev. Geophys. 50, 1–72. https://doi.org/10.1029/2011RG000371.
Carlson, A.E., Clark, P.U., Haley, B.A., Klinkhammer, G.P., Simmons, K., Brook, E.J., Meissner, K.J., 2007. Geochemical proxies of North American freshwater routing during the Younger Dryas cold event. Proc. Natl. Acad. Sci. U. S. A. 104, 6556–6561. https://doi.org/10.1073/pnas.0611313104.
Carlson, A.E., Legrande, A.N., Oppo, D.W., Came, R.E., Schmidt, G.A., Anslow, F.S., Licciardi, J.M., Obbink, E.A., 2008a. Rapid early Holocene deglaciation of the Laurentide ice sheet. Nat. Geosci. 1, 620–624. https://doi.org/10.1038/ngeo285.
Carlson, A.E., Oppo, D.W., Came, R.E., LeGrande, A.N., Keigwin, L.D., Curry, W.B., 2008b. Subtropical Atlantic salinity variability and Atlantic meridional circulation during the last deglaciation. Geology 36, 991–994.
Carroll, J., Falkner, K.K., Brown, E.T., Moore, W.S., 1993. The role of the Ganges-Brahmaputra mixing zone in supplying barium and ^{226}Ra to the Bay of Bengal. Geochim. Cosmochim. Acta 57, 2981–2990. https://doi.org/10.1016/0016-7037(93)90287-7.
Clark, J.A., Hendriks, M., Timmermans, T.J., Struck, C., Hilverda, K.J., 1994. Glacial isostatic deformation of the Great-Lakes region. Geol. Soc. Am. Bull. 106, 19–31. https://doi.org/10.1130/0016-7606(1994)106<0019:GIDOTG>2.3.CO;2.
Clark, P.U., Dyke, A.S., Shakun, J.D., Carlson, A.E., Clark, J., Wohlfarth, B., Mitrovica, J.X., Hostetler, S.W., McCabe, A.M., 2009. The Last Glacial Maximum. Science 325, 710–714. https://doi.org/10.1126/science.1172873.
Clark, P.U., Marshall, S.J., Clarke, G.K.C., Hostetler, S.W., Licciardi, J.M., Teller, J.T., 2001. Freshwater forcing of abrupt climate change during the last glaciation. Science 293, 283–287. https://doi.org/10.1126/science.1062517.
Coffey, M., Dehairs, F., Collette, O., Luther, G., Church, T., Jickells, T., 1997. The behaviour of dissolved barium in estuaries. Estuarine. Coast. Shelf Sci. 45, 113–121. https://doi.org/10.1006/ecss.1996.0157.
Cortijo, E., Duplessy, J., Labeyrie, L., Leclaire, H., Duprat, J., Van Weering, T., 1994. Eemian cooling in the Norwegian Sea and North Atlantic ocean preceding continental ice-sheet growth. Nature 372, 446–449. https://doi.org/10.1038/372446a0.
Cortijo, E., Lehman, S., Keigwin, L., Chapman, M., Paillard, D., Labeyrie, L., 1999. Changes in meridional temperature and salinity gradients in the North Atlantic ocean (30°–72°N) during the last interglacial period. Paleoceanography 14, 23–33. https://doi.org/10.1029/1998PA900004.
Deschamps, P., Durand, N., Bard, E., Hamelin, B., Camoin, G., Thomas, A.L., Henderson, G.M., Okuno, J.i., Yokoyama, Y., 2012. Ice-sheet collapse and sea-level rise at the Bølling warming 14,600 years ago. Nature 483, 559–564. https://doi.org/10.1038/nature10902.
Eggins, S., De Deckker, P., Marshall, J., 2003. Mg/Ca variation in planktonic foraminifera tests: implications for reconstructing palaeo-seawater temperature and habitat migration. Earth Planet. Sci. Lett. 212, 291–306. https://doi.org/10.1016/s0012-821x(03)00283-8.
Ekaykin, A.A., Lipenkov, V.Y., Barkov, N.I., Petit, J.R., Masson-Delmotte, V., 2002. Spatial and temporal variability in isotope composition of recent snow in the vicinity of Vostok station, Antarctica: implications for ice-core record interpretation. Ann. Glaciol. 35, 181–186. https://doi.org/10.3189/172756402781816726.
Eyles, N., Schwarcz, H.P., 1991. Stable isotope record of the last glacial cycle from lacustrine ostracodes. Geology 19, 257–260. https://doi.org/10.1130/0091-7613(1991).
Fairbanks, R.G., 1989. A 17,000-year glacio-eustatic sea level record–influence of glacial melting rates on the Younger Dryas event and deep ocean circulation. Nature 342, 637–642. https://doi.org/10.1038/342637a0.
Fairbanks, R.G., Charles, C.D., Wright, J.D., 1992. Origin of global meltwater pulses. In: Taylor, R.E., Long, A., Kra, R.S. (Eds.), Radiocarbon after Four Decades: an Interdisciplinary Perspective. Springer-Verlag, New York, pp. 473–500.
Fairbanks, R.G., Sverdlove, M., Free, R., Wiebe, P.H., Bé, A.W.H., 1982. Vertical distribution and isotopic fractionation of living planktonic foraminifera from the Panama Basin. Nature 298, 841–844. https://doi.org/10.1038/298841a0.
Fehrenbacher, J.S., Spero, H.J., Russell, A.D., Vetter, L., Eggins, S., 2015. Optimizing LA-ICP-MS analytical procedures for elemental depth profiling of foraminiferal calcite. Chem. Geol. 407–408, 2–9. https://doi.org/10.1016/j.chemgeo.2015.04.007.
Ferguson, G., Jasechko, S., 2015. The isotopic composition of the Laurentide Ice Sheet and fossil groundwater. Geophys. Res. Lett. 42, 4856–4861. https://doi.org/10.1002/2015GL064106.
Flower, B.P., Hastings, D.W., Hill, H.W., Quinn, T.M., 2004. Phasing of deglacial warming and Laurentide Ice Sheet meltwater in the Gulf of Mexico. Geology 32, 597–600. https://doi.org/10.1130/G20604.1.
Flower, B.P., Williams, C., Hill, H.W., Hastings, D.W., 2011. Laurentide Ice Sheet meltwater and the Atlantic Meridional Overturning Circulation during the last glacial cycle: a view from the Gulf of Mexico. In: Rashid, H., Polyak, L., Mosley-Thompson, E. (Eds.), Abrupt Climate Change: Mechanisms, Patterns, and Impacts. AGU, Washington, DC, pp. 39–56.
Ford, H.L., Ravelo, A.C., Polissar, P.J., 2015. Reduced El Niño - Southern Oscillation during the Last Glacial Maximum. Science 347, 255–258. https://doi.org/10.1126/science.1258437.
Gregoire, L.J., Payne, A.J., Valdes, P.J., 2012. Deglacial rapid sea level rises caused by ice-sheet saddle collapses. Nature 487, 219–222. https://doi.org/10.1038/nature11257.
Guay, C.K., Falkner, K., 1997. Barium as a tracer of Arctic halocline and river waters. Deep Sea Res. Part II Top. Stud. Oceanogr. 44, 1543–1569. https://doi.org/10.1016/S0967-0645(97)00066-0.
Hall, J.M., Chan, L.H., 2004. Ba/Ca in *Neogloboquadrina pachyderma* as an indicator of deglacial meltwater discharge into the western Arctic Ocean. Paleoceanography 19, PA1017. https://doi.org/10.1029/2003pa000910.
Hanor, J.S., Chan, L.H., 1977. Non-conservative behavior of barium during mixing of Mississippi River and Gulf of Mexico waters. Earth Planet. Sci. Lett. 37, 242–250. https://doi.org/10.1016/0012-821X(77)90169-8.
Hill, H.W., Flower, B.P., Quinn, T.M., Hollander, D.J., Guilderson, T.P., 2006. Laurentide Ice Sheet meltwater and abrupt climate change during the last glaciation. Paleoceanography 21, PA1006. https://doi.org/10.1029/2005PA001186.
Hillaire-Marcel, C., Causse, C., 1989. The late Pleistocene Laurentide glacier–Th/U dating of its major fluctuations and delta-O-18 range of the ice. Quat. Res. 32, 125–138. https://doi.org/10.1139/e89-085.
Hillaire-Marcel, C., Soucy, J.M., Cailleux, A., 1979. Isotopic analysis of subglacial concretions of Laurentide Ice Sheet and O-18 content of ice. Can. J. Earth Sci. 16, 1494–1498. https://doi.org/10.1139/E08-029.
Hladyniuk, R., Longstaffe, F.J., 2016. Oxygen-isotope variations in post-glacial Lake Ontario. Quat. Sci. Rev. 134, 39–50. https://doi.org/10.1029/98JD00423.
Hoffman, J.S., Carlson, A.E., Winsor, K., Klinkhammer, G.P., LeGrande, A.N., Andrews, J.T., Strasser, J.C., 2012. Linking the 8.2 ka event and its freshwater forcing in the Labrador Sea. Geophys. Res. Lett. 39, L18703. https://doi.org/10.1029/2012gl053047.
Hoffmann, G., Werner, M., Heimann, M., 1998. Water isotope module of the ECHAM atmospheric general circulation model: a study on timescales from days to several years. J. Geophys. Res. Atmos. 103, 16871–16896. https://doi.org/10.1029/98JD00423.
Hönisch, B., Allen, K.A., Russell, A.D., Eggins, S.M., Bijma, J., Spero, H.J., Lea, D.W., Yu, J., 2011. Planktic foraminifers as recorders of seawater Ba/Ca. Mar. Micropaleontol. 79, 52–57. https://doi.org/10.1016/j.marmicro.2011.01.003.
Hooke, R.L., 1976. Pleistocene ice at the base of the Barnes Ice Cap, Baffin Island, N.W.T., Canada. J. Glaciol. 17, 49–59.
Hooke, R.L., Clausen, H.B., 1982. Wisconsin and Holocene δ^{18}O variations, Barnes Ice Cap, Canada. Geol. Soc. Am. Bull. 93, 784–789. https://doi.org/10.1130/0016-7606(1982)93<784:WAHOVB>2.0.CO;2.
Irvalı, N., Ninnemann, U.S., Galaasen, E.V., Rosenthal, Y., Kroon, D., Oppo, D.W., Kleiven, H.F., Darling, K.F., Kissel, C., 2012. Rapid switches in subpolar North Atlantic hydrography and climate during the Last Interglacial (MIS 5e). Paleoceanography 27, PA2207. https://doi.org/10.1029/2011PA002244.
Jasechko, S., Lechler, A., Pausata, F.S., Fawcett, P.J., Gleeson, T., Cendón, D.I., Galewsky, J., LeGrande, A.N., Risi, C., Sharp, Z.D., 2015. Late-glacial to late-Holocene shifts in global precipitation δ^{18}O. Clim. Past 11, 1375. https://doi.org/10.5194/cp-11-1375-2015.
Johnsen, S.J., Dansgaard, W., Clausen, H.B., Langway, C.C., 1972. Oxygen isotope profiles through Antarctic and Greenland ice sheets. Nature 235, 429–434. https://doi.org/10.1038/235429a0.
Joung, D., Shiller, A.M., 2014. Dissolved barium behavior in Louisiana Shelf waters affected by the Mississippi/Atchafalaya River mixing zone. Geochim. Cosmochim. Acta 141, 303–313. https://doi.org/10.1016/j.gca.2014.06.021.
Kehew, A.E., Teller, J.T., 1994. History of late-glacial runoff along the southwestern margin of the Laurentide ice-sheet. Quat. Sci. Rev. 13, 859–877. https://doi.org/10.1016/0277-3791(94)90006-X.
Keigwin, L.D., Jones, G.A., Lehman, S.J., Boyle, E.A., 1991. Deglacial meltwater discharge, North Atlantic deep circulation, and abrupt climate change. J. Geophys. Res.-Oceans 96, 16811–16826.
Kennett, J.P., Elmstrom, K., Penrose, N., 1985. The last deglaciation in Orca Basin, Gulf of Mexico: high-resolution planktonic foraminiferal changes. Palaeogeogr. Palaeoclimatol. Palaeoecol. 50, 189–216. https://doi.org/10.1016/S0031-0182(85)80013-4.
Kennett, J.P., Shackleton, N.J., 1975. Laurentide ice sheet meltwater recorded in Gulf of Mexico deep sea cores. Science 188, 147–150. https://doi.org/10.1126/science.188.4184.147.
Kleman, J., Fastook, J., Stroeven, A.P., 2002. Geologically and geomorphologically constrained numerical model of Laurentide Ice Sheet inception and build-up. Quat. Int. 95–6, 87–98. https://doi.org/10.1130/G22810A.1.
Kotler, E., Burn, C.R., 2000. Cryostratigraphy of the klondike "muck" deposits, west-central Yukon Territory. Can. J. Earth Sci. 37, 849–861. https://doi.org/10.1139/

e00-013.
Koutavas, A., deMenocal, P.B., Olive, G.C., Lynch-Stieglitz, J., 2006. Mid-Holocene El Niño-Southern Oscillation (ENSO) attenuation revealed by individual foraminifera in eastern tropical Pacific sediments. Geology 34, 993–996. https://doi.org/10.1130/G22810A.1.
Koutavas, A., Joanides, S., 2012. El Niño-Southern Oscillation extrema in the Holocene and Last Glacial Maximum. Paleoceanography 27, PA4208. https://doi.org/10.1029/2012PA002378.
Lambeck, K., Yokoyama, Y., Purcell, T., 2002. Into and out of the last glacial maximum: sea-level change during oxygen isotope stages 3 and 2. Quat. Sci. Rev. 21, 343–360. https://doi.org/10.1016/s0277-3791(01)00071-3.
Last, W.M., Teller, J.T., Forester, R.M., 1994. Paleohydrology and paleochemistry of Lake Manitoba, Canada: the isotope and ostracode records. J. Paleolimnol. 12, 269–282. https://doi.org/10.1007/BF00678025.
Lea, D.W., Boyle, E.A., 1991. Barium in planktonic foraminifera. Geochim. Cosmochim. Acta 55, 3321–3331. https://doi.org/10.1016/0016-7037(91)90491-M.
Lea, D.W., Mashiotta, T.A., Spero, H.J., 1999. Controls on magnesium and strontium uptake in planktonic foraminifera determined by live culturing. Geochim. Cosmochim. Acta 63, 2369–2379. https://doi.org/10.1016/S0016-7037(99)00197-0.
Lea, D.W., Pak, D.K., Spero, H.J., 2000. Climate impact of Late Quaternary equatorial Pacific sea surface temperature variations. Science 289, 1719–1724. https://doi.org/10.1126/science.289.5485.1719.
Lea, D.W., Spero, H.J., 1992. Experimental determination of barium uptake in shells of the planktonic foraminifera *Orbulina universa* at 22°C. Geochim. Cosmochim. Acta 56, 2673–2680.
Lea, D.W., Spero, H.J., 1994. Assessing the reliability of paleochemical tracers: barium uptake in the shells of planktonic foraminifera. Paleoceanography 9, 445–452.
LeGrande, A.N., Schmidt, G.A., Shindell, D.T., Field, C.V., Miller, R.L., Koch, D.M., Faluvegi, G., Hoffmann, G., 2006. Consistent simulations of multiple proxy responses to an abrupt climate change event. Proc. Natl. Acad. Sci. U. S. A. 103, 837–842. https://doi.org/10.1073/pnas.0510095103.
Leventer, A., Williams, D.F., Kennett, J.P., 1982. Dynamics of the Laurentide Ice Sheet during the last deglaciation–evidence from the Gulf of Mexico. Earth Planet. Sci. Lett. 59, 11–17. https://doi.org/10.1016/0012-821X(82)90112-1.
Licciardi, J.M., Teller, J.T., Clark, P.U., 1999. Freshwater routing by the Laurentide Ice Sheet during the last deglaciation. In: Clark, P.U., Webb, R.S., Keigwin, L.D. (Eds.), Mechanisms of Global Climate Change at Millennial Timescales. American Geophysical Union, Washington, D.C, pp. 177–202.
Marchitto, T.M., Wei, K.-Y., 1995. History of Laurentide meltwater flow to the Gulf of Mexico during the last deglaciation, as revealed by reworked calcareous nannofossils. Geology 23, 779–782. https://doi.org/10.1130/0091-7613(1995).
Marshall, S.J., Tarasov, L., Clarke, G.K.C., Peltier, W.R., 2000. Glaciological reconstruction of the Laurentide Ice Sheet: physical processes and modelling challenges. Can. J. Earth Sci. 37, 769–793. https://doi.org/10.1139/e99-113.
Masson-Delmotte, V., Hou, S., Ekaykin, A., Jouzel, J., Aristarain, A., Bernardo, R., Bromwich, D., Cattani, O., Delmotte, M., Falourd, S., 2008. A review of Antarctic surface snow isotopic composition: observations, atmospheric circulation, and isotopic modeling*. J. Clim. 21, 3359–3387. https://doi.org/10.1175/2007JCLI2139.1.
Meckler, A.N., Schubert, C.J., Hochuli, P.A., Plessen, B., Birgel, D., Flower, B.P., Hinrichs, K.U., Haug, G.H., 2008. Glacial to Holocene terrigenous organic matter input to sediments from Orca Basin, Gulf of Mexico - a combined optical and biomarker approach. Earth Planet. Sci. Lett. 272, 251–263. https://doi.org/10.1016/j.epsl.2008.04.046.
Montero-Serrano, J.C., Bout-Roumazeilles, V., Tribovillard, N., Sionneau, T., Riboulleau, A., Bory, A., Flower, B., 2009. Sedimentary evidence of deglacial megafloods in the northern Gulf of Mexico (Pigmy Basin). Quat. Sci. Rev. 28, 3333–3347. https://doi.org/10.1016/j.quascirev.2009.09.011.
Moore, T.C., Walker, J.C.G., Rea, D.K., Lewis, C.F.M., Shane, L.C.K., Smith, A.J., 2000. Younger Dryas interval and outflow from the Laurentide Ice Sheet. Paleoceanography 15, 4–18. https://doi.org/10.1029/1999PA000437.
Mora, G., Martínez, J.I., 2005. Sedimentary metal ratios in the Colombia Basin as indicators for water balance change in northern South America during the past 400,000 years. Paleoceanography 20, PA4013. https://doi.org/10.1029/2005pa001132.
Morgan, V.I., 1982. Antarctic Ice Sheet surface oxygen isotope values. J. Glaciol. 28, 315–323. https://doi.org/10.3198/1982JoG28-99-315-323.
Obbink, E.A., Carlson, A.E., Klinkhammer, G.P., 2010. Eastern North American freshwater discharge during the Bølling-Allerød warm periods. Geology 38, 171–174. https://doi.org/10.1130/g30389.1.
Oerlemans, J., 1982. Glacial cycles and ice-sheet modelling. Clim. Change 4, 353–374. https://doi.org/10.1007/BF00142535.
Oster, J.L., Ibarra, D.E., Winnick, M.J., Maher, K., 2015. Steering of westerly storms over western North America at the last glacial maximum. Nat. Geosci. 8, 201–205. https://doi.org/10.1038/ngeo2365.
Pausata, F.S.R., Battisti, D.S., Nisancioglu, K.H., Bitz, C.M., 2011. Chinese stalagmite $\delta^{18}O$ controlled by changes in the Indian monsoon during a simulated Heinrich event. Nat. Geosci. 4, 474–480. https://doi.org/10.1038/ngeo1169.
Peltier, W., Argus, D., Drummond, R., 2015. Space geodesy constrains ice age terminal deglaciation: the global ICE-6G_C (VM5a) model. J. Geophys. Res. Solid Earth 120, 450–487. https://doi.org/10.1002/2014JB011176.
Plewa, K., Meggers, H., Kasten, S., 2006. Barium in sediments off northwest Africa: a tracer for paleoproductivity or meltwater events? Paleoceanography 21. https://doi.org/10.1029/2005PA001136.
Refsnider, K.A., Miller, G.H., Fogel, M.L., Fréchette, B., Bowden, R., Andrews, J.T., Farmer, G.L., 2014. Subglacially precipitated carbonates record geochemical interactions and pollen preservation at the base of the Laurentide Ice Sheet on central Baffin Island, eastern Canadian Arctic. Quat. Res. 81, 94–105. https://doi.org/10.1016/j.yqres.2013.10.014.
Refsnider, K.A., Miller, G.H., Hillaire-Marcel, C., Fogel, M.L., Ghaleb, B., Bowden, R., 2012. Subglacial carbonates constrain basal conditions and oxygen isotopic composition of the Laurentide Ice Sheet over Arctic Canada. Geology 40, 135–138. https://doi.org/10.1130/g32335.1.
Remenda, V.H., Cherry, J.A., Edwards, T.W.D., 1994. Isotopic composition of old ground water from Lake Agassiz: implications for Late Pleistocene climate. Science 266, 1975–1978. https://doi.org/10.1126/science.266.5193.1975.
Risi, C., Bony, S., Vimeux, F., Jouzel, J., 2010. Water-stable isotopes in the LMDZ4 general circulation model: model evaluation for present-day and past climates and applications to climatic interpretations of tropical isotopic records. J. Geophys. Res. Atmos. 115 https://doi.org/10.1029/2009JD013255 n/a-n/a.
Rohling, E.J., 2000. Paleosalinity: confidence limits and future applications. Mar. Geol. 163, 1–11. https://doi.org/10.1016/S0025-3227(99)00097-3.
Russell, A.D., Hönisch, B., Spero, H.J., Lea, D.W., 2004. Effects of seawater carbonate ion concentration and temperature on shell U, Mg, and Sr in cultured planktonic foraminifera. Geochim. Cosmochim. Acta 68, 4347–4361. https://doi.org/10.1016/j.gca.2004.03.013.
Rustic, G.T., Koutavas, A., Marchitto, T.M., Linsley, B.K., 2015. Dynamical excitation of the tropical Pacific Ocean and ENSO variability by Little Ice Age cooling. Science 350, 1537–1541. https://doi.org/10.1126/science.aac9937.
Rutt, I.C., Hagdorn, M., Hulton, N.R.J., Payne, A.J., 2009. The Glimmer community ice sheet model. J. Geophys. Research-Earth Surf. 114 https://doi.org/10.1029/2008jf001015.
Schmidt, M.W., Lynch-Stieglitz, J., 2011. Florida Straits deglacial temperature and salinity change: implications for tropical hydrologic cycle variability during the Younger Dryas. Paleoceanography 26, PA4205. https://doi.org/10.1029/2011pa002157.
Schmidt, M.W., Spero, H.J., Lea, D.W., 2004. Links between salinity variation in the Caribbean and North Atlantic thermohaline circulation. Nature 428, 160–163. https://doi.org/10.1038/nature02346.
Schmidt, M.W., Vautravers, M.J., Spero, H.J., 2006. Rapid subtropical North Atlantic salinity oscillations across Dansgaard-Oeschger cycles. Nature 443, 561–564. https://doi.org/10.1038/nature05121.
Schwarcz, H.P., Eyles, N., 1991. Laurentide ice-sheet extent inferred from stable isotopic composition (O, C) of ostracodes at Toronto, Canada. Quat. Res. 35, 305–320. https://doi.org/10.1016/0033-5894(91)90047-9.
Seierstad, I.K., Abbott, P.M., Bigler, M., Blunier, T., Bourne, A.J., Brook, E., Buchardt, S.L., Buizert, C., Clausen, H.B., Cook, E., Dahl-Jensen, D., Davies, S.M., Guillevic, M., Johnsen, S.J., Pedersen, D.S., Popp, T.J., Rasmussen, S.O., Severinghaus, J.P., Svensson, A., Vinther, B.M., 2014. Consistently dated records from the Greenland GRIP, GISP2 and NGRIP ice cores for the past 104 ka reveal regional millennial-scale $\delta^{18}O$ gradients with possible Heinrich event imprint. Quat. Sci. Rev. 106, 29–46. https://doi.org/10.1016/j.quascirev.2014.10.032.
Shiller, A.M., 1997. Dissolved trace elements in the Mississippi River: seasonal, interannual, and decadal variability. Geochim. Cosmochim. Acta 61, 4321–4330. https://doi.org/10.1016/S0016-7037(97)00245-7.
Shiller, A.M., Boyle, E.A., 1987. Variability of dissolved trace metals in the Mississippi River. Geochim. Cosmochim. Acta 51, 3273–3277. https://doi.org/10.1016/0016-7037(87)90134-7.
Sima, A., Paul, A., Schulz, M., Oerlemans, J., 2006. Modeling the oxygen-isotopic composition of the North American Ice Sheet and its effect on the isotopic composition of the ocean during the last glacial cycle. Geophys. Res. Lett. 33, 5. L1570610. 1029/2006gl026923.
Sionneau, T., Bout-Roumazeilles, V., Flower, B.P., Bory, A., Tribovillard, N., Kissel, C., Van Vliet-Lanoe, B., Serrano, J.C.M., 2010. Provenance of freshwater pulses in the Gulf of Mexico during the last deglaciation. Quat. Res. 74, 235–245. https://doi.org/10.1016/j.yqres.2010.07.002.
Spear, J.W., Reynolds, C.E., Poore, R.Z., 2011. Seasonal Flux and Assemblage Composition of Planktic Foraminifera from the Northern Gulf of Mexico, 2008-2010. US Geological Survey Open File Report 2011-1215, pp. 1–16.
Spero, H.J., 1988. Ultrastructural examination of chamber morphogenesis and biomineralization in the planktonic foraminifer *Orbulina universa*. Mar. Biol. 99, 9–20. https://doi.org/10.1007/BF00644972.
Spero, H.J., Williams, D.F., 1990. Evidence for seasonal low-salinity surface waters in the Gulf of Mexico over the last 16,000 years. Paleoceanography 5, 963–975. https://doi.org/10.1029/PA005i006p00963.
Sprovieri, M., d'Alcala, M.R., Manta, D.S., Bellanca, A., Neri, R., Lirer, F., Taberner, C., Jose Pueyo, J., Sammartino, S., 2008. Ba/Ca evolution in water masses of the Mediterranean Late Neogene. Paleoceanography 23. https://doi.org/10.1029/2007pa001469.
Stenni, B., Masson-Delmotte, V., Johnsen, S., Jouzel, J., Longinelli, A., Monnin, E., Röthlisberger, R., Selmo, E., 2001. An oceanic cold reversal during the last deglaciation. Science 293, 2074–2077. https://doi.org/10.1126/science.1059702.
Tarasov, L., Peltier, W.R., 2004. A geophysically constrained large ensemble analysis of the deglacial history of the North American ice-sheet complex. Quat. Sci. Rev. 23, 359–388. https://doi.org/10.1016/j.quascirev.2003.08.004.
Teller, J.T., 1990a. Meltwater and precipitation runoff to the North Atlantic, Arctic, and Gulf of Mexico from the Laurentide Ice Sheet and adjacent regions during the Younger Dryas. Paleoceanography 5, 897–905.

Teller, J.T., 1990b. Volume and routing of late-glacial runoff from the southern Laurentide Ice Sheet. Quat. Res. 34, 12–23.
Teller, J.T., Kehew, A.E., 1994. Introduction to the late glacial history of large proglacial lakes and meltwater runoff along the Laurentide Ice Sheet. Quat. Sci. Rev. 13, 795–799. https://doi.org/10.1016/0277-3791(94)90001-9.
Thornalley, D.J.R., Elderfield, H., McCave, I.N., 2011. Reconstructing North Atlantic deglacial surface hydrography and its link to the Atlantic overturning circulation. Glob. Planet. Change 79, 163–175. https://doi.org/10.1016/j.gloplacha.2010.06.003.
Thornalley, D.J.R., McCave, I.N., Elderfield, H., 2010. Freshwater input and abrupt deglacial climate change in the North Atlantic. Paleoceanography 25, PA1201. https://doi.org/10.1029/2009pa001772.
Ullman, D.J., LeGrande, A.N., Carlson, A.E., Anslow, F.S., Licciardi, J.M., 2014. Assessing the impact of Laurentide Ice Sheet topography on glacial climate. Clim. Past. 10, 487–507. https://doi.org/10.5194/cp-10-487-2014.
Vetter, L., Kozdon, R., Mora, C.I., Eggins, S.M., Valley, J.W., Hönisch, B., Spero, H.J., 2013a. Micron-scale intrashell oxygen isotope variation in cultured planktic foraminifers. Geochim. Cosmochim. Acta 107, 267–278. https://doi.org/10.1016/j.gca.2012.12.046.
Vetter, L., Spero, H.J., Russell, A.D., Fehrenbacher, J.S., 2013b. LA-ICP-MS depth profiling perspective on cleaning protocols for elemental analyses in planktic foraminifers. Geochem. Geophys. Geosys 14, 2916–2931. https://doi.org/10.1002/ggge.20163.
Vinther, B.M., Buchardt, S.L., Clausen, H.B., Dahl-Jensen, D., Johnsen, S.J., Fisher, D.A., Koerner, R.M., Raynaud, D., Lipenkov, V., Andersen, K.K., Blunier, T., Rasmussen, S.O., Steffensen, J.P., Svensson, A.M., 2009. Holocene thinning of the Greenland ice sheet. Nature 461, 385–388.
Watanabe, T., Winter, A., Oba, T., 2001. Seasonal changes in sea surface temperature and salinity during the Little Ice Age in the Caribbean Sea deduced from Mg/Ca and $^{18}O/^{16}O$ ratios in corals. Mar. Geol. 173, 21–35. https://doi.org/10.1016/S0025-3227(00)00166-3.
Weldeab, S., Lea, D.W., Schneider, R.R., Andersen, N., 2007. 155,000 years of West African monsoon and ocean thermal evolution. Science 316, 1303–1307. https://doi.org/10.1126/science.1140461.
Werner, M., Langebroek, P.M., Carlsen, T., Herold, M., Lohmann, G., 2011. Stable water isotopes in the ECHAM5 general circulation model: toward high-resolution isotope modeling on a global scale. J. Geophys. Res. 116, 1–14. https://doi.org/10.1029/2011JD015681.
Wickert, A.D., 2016. Reconstruction of North American drainage basins and river discharge since the last glacial maximum. Earth Surf. Dyn. 4, 831. https://doi.org/10.5194/esurf-4-831-2016.
Wickert, A.D., Mitrovica, J.X., Williams, C., Anderson, R.S., 2013. Gradual demise of a thin southern Laurentide ice sheet recorded by Mississippi drainage. Nature 502, 668–671. https://doi.org/10.1038/nature12609.
Williams, C., Flower, B.P., Hastings, D.W., 2012. Seasonal Laurentide Ice Sheet melting during the “Mystery Interval” (17.5–14.5 ka). Geology. https://doi.org/10.1130/g33279.1.
Williams, C., Flower, B.P., Hastings, D.W., Guilderson, T.P., Quinn, K.A., Goddard, E.A., 2010. Deglacial abrupt climate change in the Atlantic Warm Pool: a Gulf of Mexico perspective. Paleoceanography 25. https://doi.org/10.1029/2010pa001928.
Winsor, K., Carlson, A.E., Klinkhammer, G.P., Stoner, J.S., Hatfield, R.G., 2012. Evolution of the northeast Labrador Sea during the last interglaciation. Geochem. Geophys. Geosystems 13. https://doi.org/10.1029/2012GC004263 n/a-n/a.
Wolf-Gladrow, D.A., Bijma, J., Zeebe, R.E., 1999. Model simulation of the carbonate chemistry in the microenvironment of symbiont bearing foraminifera. Mar. Chem. 64, 181–198. https://doi.org/10.1016/s0304-4203(98)00074-7.
York, D., Evensen, N.M., Martínez, M.L., De Basabe Delgado, J., 2004. Unified equations for the slope, intercept, and standard errors of the best straight line. Am. J. Phys. 72, 367–375. https://doi.org/10.1119/1.1632486.
Yoshimura, K., Kanamitsu, M., Noone, D., Oki, T., 2008. Historical isotope simulation using Reanalysis atmospheric data. J. Geophys. Res. Atmos. 113, 1–15. https://doi.org/10.1029/2008JD010074.

Supplemental Information.
Vetter, L. et al., Quaternary Science Reviews, 2017.

FIGURE S-1. Modern examples of $\delta^{18}O_{sw}$ vs. salinity relationships from both open-ocean settings and locations influenced by precipitation and/or glacial runoff. Modified from Fairbanks et al., (1992).

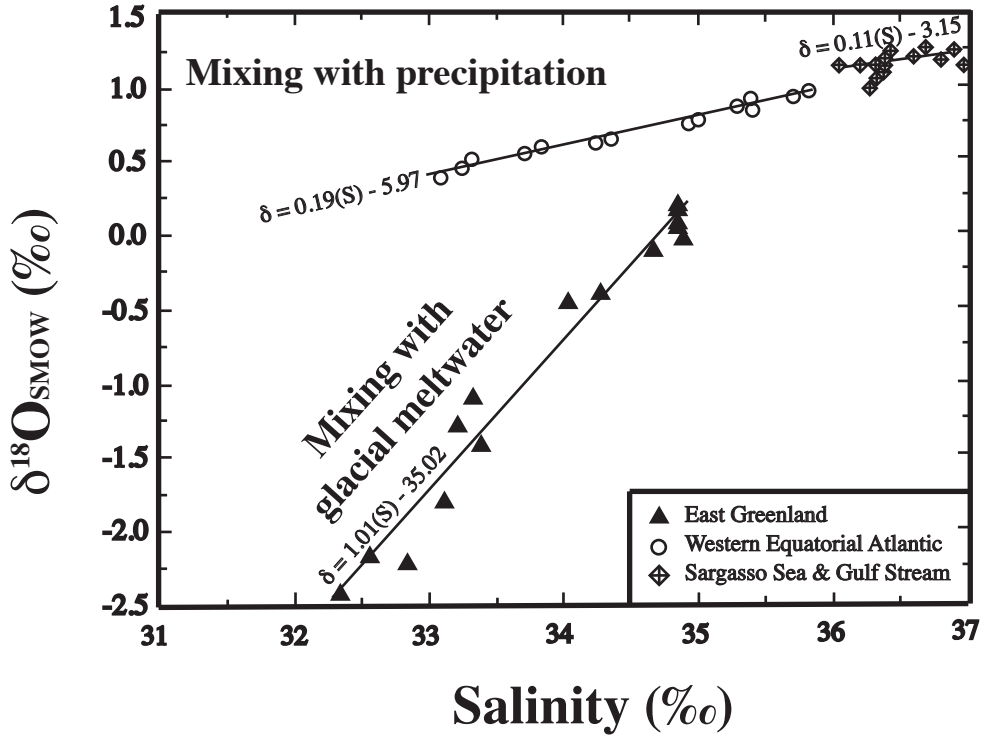

Supplemental Information.
Vetter, L. et al., Quaternary Science Reviews, 2017.

FIGURE S-2. Basin-specific Ba-salinity relationships in global rivers

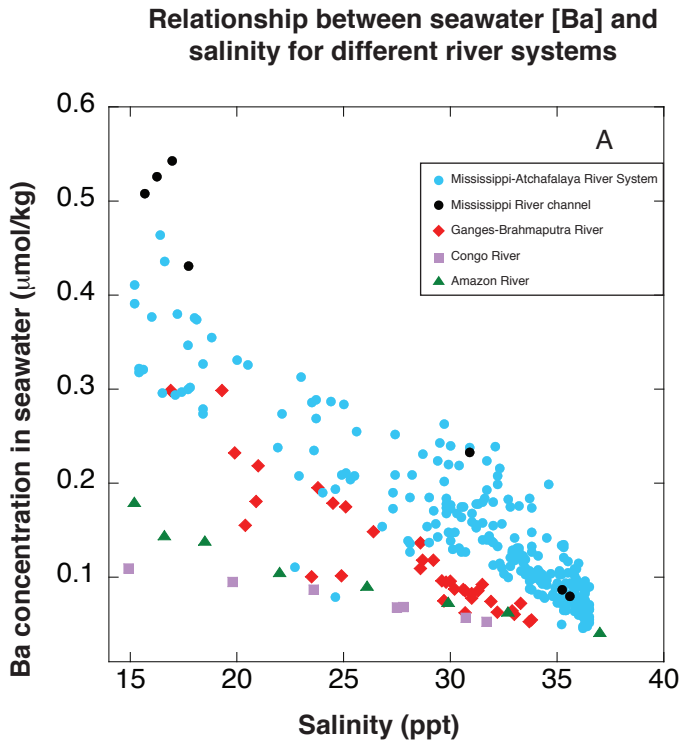

(A) Salinity and [Ba] concentration data measured for 4 different global rivers, showing basin-specific empirical relationships. The Mississippi-Atchafalaya River system (light blue dots from Joung and Shiller, 2014; black dots from Hanor and Chan, 1977); the Ganges-Brahmaputra (red diamonds; Carroll et al., 1993); the Amazon (green triangles; Boyle, 1976); and the Congo River (purple squares; Edmond et al., 1978). Each river basin yields a different empirical relationship between Ba and salinity.

While it is possible that the Mississippi River drainage basin may have had a different S vs. Ba/Ca_{sw} relationship in the past, in this study we use the relationship based on modern measurements as a first approximation, for lack of a better substitute. We note that if the modern relationship differed substantially from the relationship during Termination I, salinity estimates from measured Ba/Ca_{shell} would not fall within the salinity tolerance of *O. universa*.

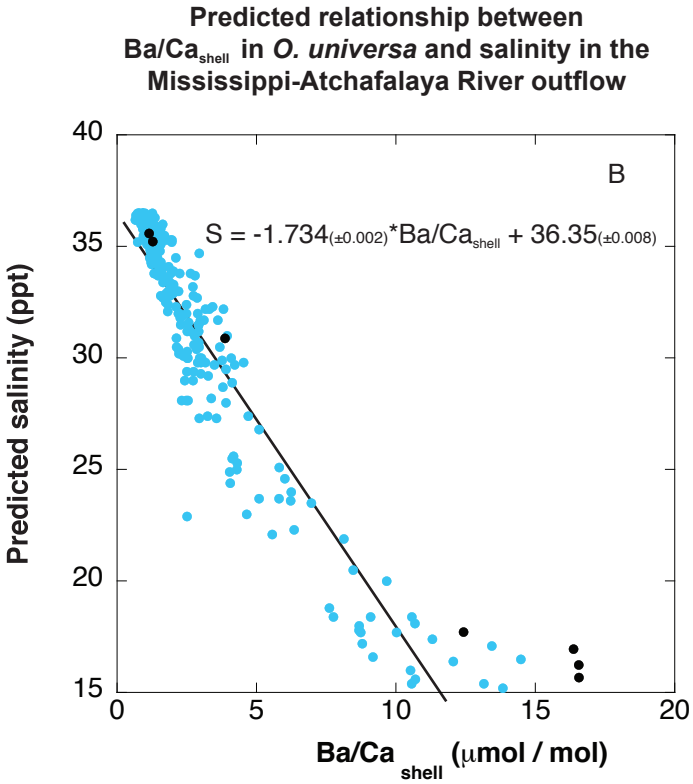

(B) Relationship between measured Ba/Ca_{shell} in *Orbulina universa* and salinity for the Gulf of Mexico influenced by freshwater from the Mississippi River. Here we use the empirical relationship between Ba/Ca_{sw} and salinity, from measurements in the Mississippi-Atchafalaya River system (A). Black dots are Ba/Ca_{sw} measurements from Hanor and Chan (1977) in the Mississippi River channel; light blue dots are Ba/Ca_{sw} measurements made by Joung and Shiller (2014) across the entire Mississippi-Atchafalaya River outflow.

For data points ≤ 15 ppt, measured Ba/Ca_{sw} were converted to Ba/Ca_{shell} using the relationship of Hönisch et al. (2011). This yields a regression equation shown, which we used as a predictive relationship between Ba/Ca_{shell} and salinity (eq. 4, Section 2.2 in main text).

Supplemental Information.
Vetter, L. et al., Quaternary Science Reviews, 2017.

Figure S-3. Intrashell trace element depth profiles from LA-ICP-MS

Examples of trace element depth profiles through individual *O. universa* shells, collected via laser ablation ICP-MS. For data reduction protocols and evaluation of specimens for potential contamination, we monitor ^{27}Al (clay contaminants), ^{43}Ca (to show intensities of ablated calcite), and ^{138}Ba (intrashell traces are homogeneous in unaltered specimens). See Section 2.3 in main text for discussion.

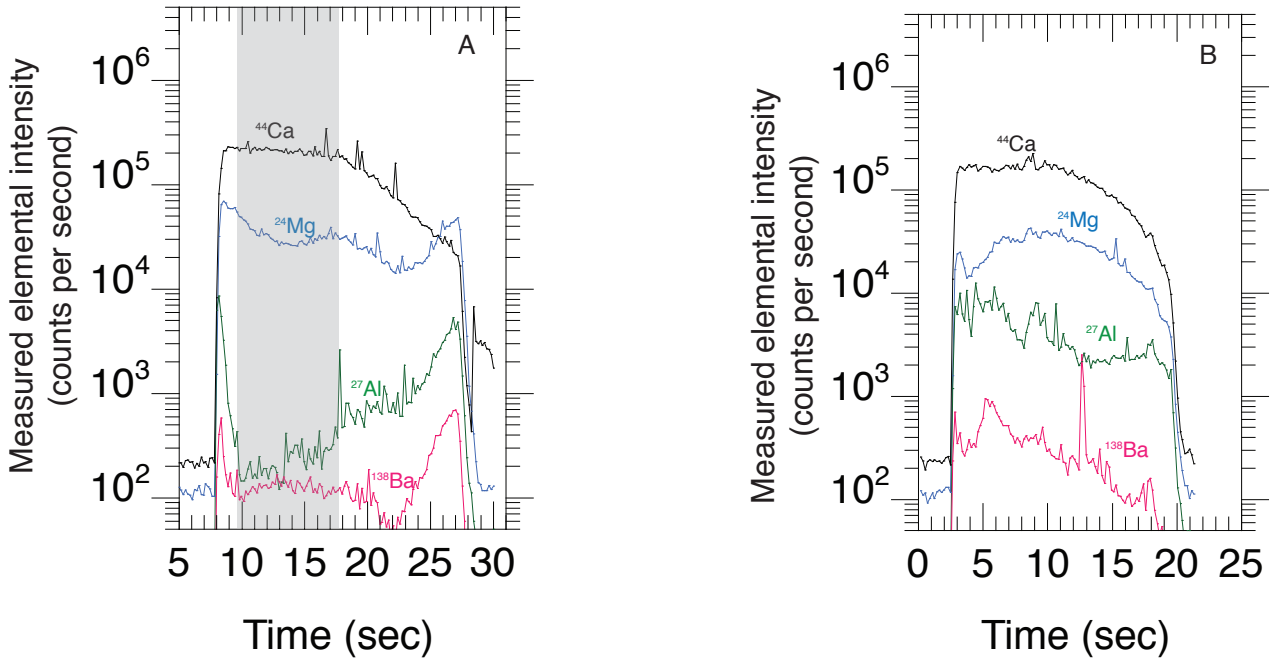

(A) shows a typical depth profile through a foraminifera shell. Shaded grey box shows the points used in determining trace element ratios for this laser ablation spot. Characteristics of a depth profile across an unaltered shell include counts of ^{44}Ca slowly decreasing with progressive ablation, low ^{27}Al (green) (Al/Ca $\leq$ 0.5 mmol mol^{-1}), and constant intrashell Ba/Ca (pink). Data outside the grey box (> 18 s) shows where the ablating laser broke through the shell, indicated by increasing ^{27}Al and an inflection point in the decrease of ^{44}Ca.

In contrast, **(B)** shows elevated ^{27}Al (green) and a heterogeneous intrashell ^{138}Ba profile (pink). These depth profiles are characteristic of adherent clays (Al) and diagenetic overprinting (Ba), and both are criteria for exclusion from the final data set we use for paleoceanographic reconstructions.

Supplemental Information.
Vetter, L. et al., Quaternary Science Reviews, 2017.

FIGURE S-4. Laser ablation data reduction protocols

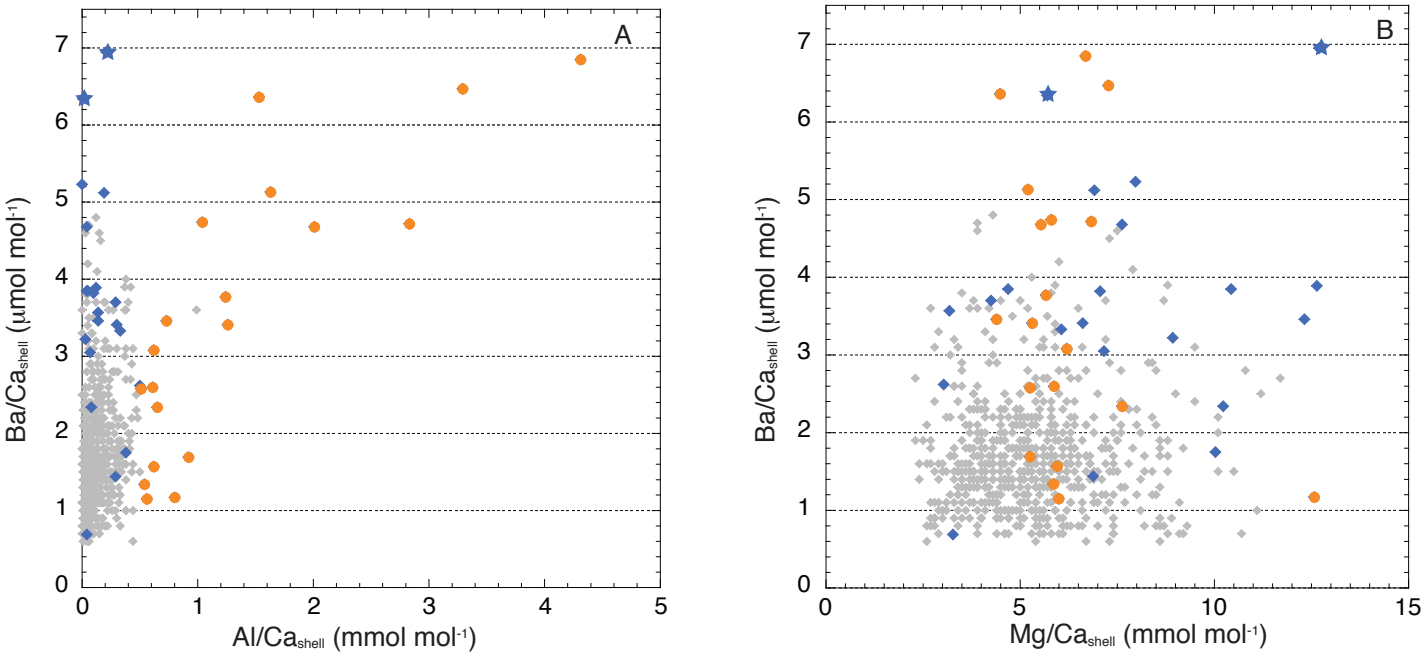

(A) Measured Al/Ca (mmol mol^{-1}) vs. measured Ba/Ca (µmol mol^{-1}) for all individual *O. universa* specimens analyzed in this study. Grey points are individual shells that were used for paleoceanographic reconstructions. Colored points are shells that were excluded from paleoceanographic reconstructions following the criteria described in Section 2.3. Orange points are specimens excluded due Al/Ca ≥ 0.5 mmol mol^{-1}. Blue points were excluded from analyses due to heterogeneous intrashell Ba/Ca, and blue stars are specimens with Ba/Ca ratios that yield salinity estimates < 30 psu. In total, 6% of analyzed specimens were removed from the dataset.

(B) Measured Mg/Ca (mmol mol^{-1}) vs. measured Ba/Ca (µmol mol^{-1}) for all individual *O. universa* specimens analyzed in this study. Grey points are individual shells that were used for paleoceanographic reconstructions. Orange points are specimens excluded due Al/Ca ≥ 0.5 mmol mol^{-1}. Blue points were excluded from analyses due to heterogeneous intrashell Ba/Ca, and blue stars are specimens with Ba/Ca ratios that yield salinity estimates < 30 psu. The colored data points (rejected) do not display covariation between Mg/Ca and Ba/Ca, suggesting little post-depositional overprinting.

Supplemental Information.
Vetter, L. et al., Quaternary Science Reviews, 2017.

FIGURE S-5. Calculated $\delta^{18}O_{sw}$ and measured Ba/Ca, Younger Dryas and Holocene time slices

Younger Dryas Cold Period, YD time slice: 12.13 - 12.17 ka

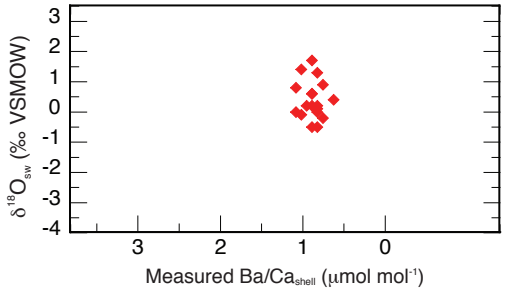

Core interval	Linear regression
353 - 353.5 cm 12.13 - 12.14 ka n = 19	no relationship

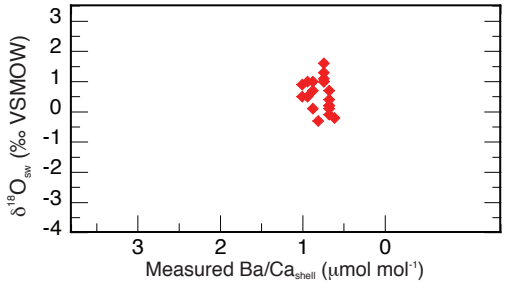

Core interval	Linear regression
353.5 - 354 cm 12.14 - 12.16 ka n = 20	no relationship

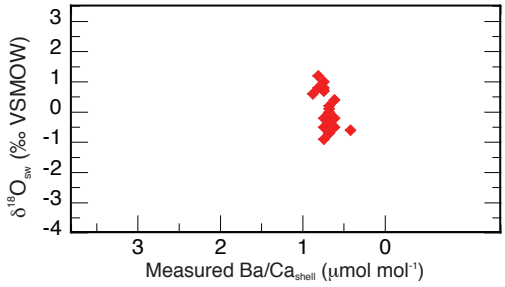

Core interval	Linear regression
354 - 354.5 cm 12.16 - 12.17 ka n = 19	no relationship

Holocene / Core Top, Late Holocene time slice

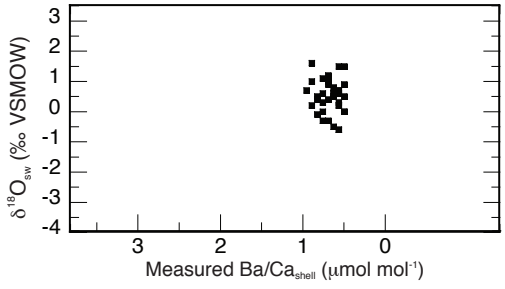

Core interval	Linear regression
20 - 22 cm near core top n = 40	no relationship

Supplemental Information.
Vetter, L. et al., Quaternary Science Reviews, 2017.

FIGURE S-6. Calculated $\delta^{18}O_{sw}$ and salinity, Bølling-Allerød Warm Period

Open-ocean
$\delta^{18}O_{sw}$ = 1.74‰
S = 37.54 psu

B_d time slice: 13.35 - 13.41 ka

	Core interval	Linear regression	Regression including open-ocean value
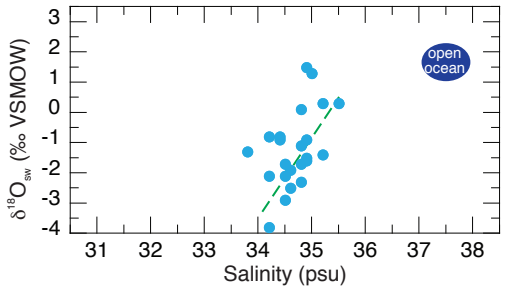	400 - 400.5 cm 13.35 - 13.37 ka n = 23	$\delta^{18}O_{sw}$ = 2.02*S - 71 (±16) r^2 = 0.00 no relationship	
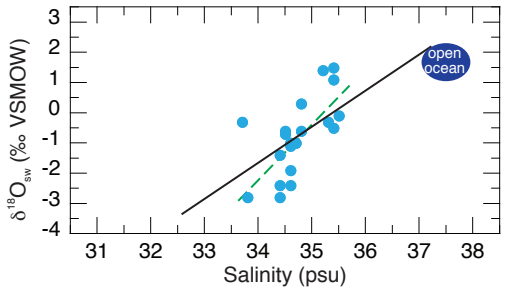	400.5 - 401 cm 13.37 - 13.38 ka n = 21	$\delta^{18}O_{sw}$ = 1.40*S - 49 (±11) r^2 = 0.37	**$\delta^{18}O_{sw}$ = 1.08*S - 38 (±8)** **r^2 = 0.46**
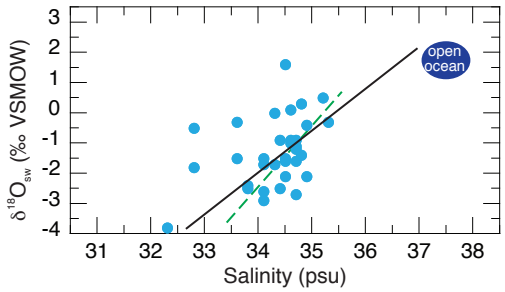	401 - 401.5 cm 13.38 - 13.40 ka n = 33	$\delta^{18}O_{sw}$ = 1.51*S - 53 (±13) r^2 = 0.04	**$\delta^{18}O_{sw}$ = 1.05*S - 37 (±7)** **r^2 = 0.08**
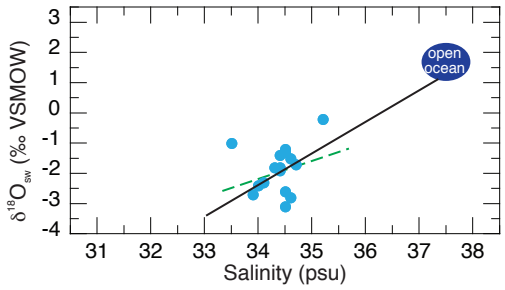	401.5 - 402 cm 13.40 - 13.41 ka n = 16	$\delta^{18}O_{sw}$ = 0.55*S - 20 (±16) r^2 = 0.06	**$\delta^{18}O_{sw}$ = 0.95*S - 31 (±8)** **r^2 = 0.64**
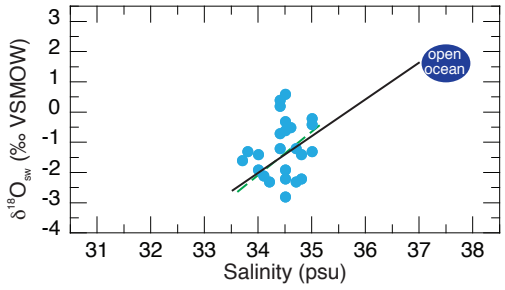	402 - 402.5 cm 13.41 - 13.43 ka n = 24	$\delta^{18}O_{sw}$ = 1.06*S - 37 (±16) r^2 = 0.07	**$\delta^{18}O_{sw}$ = 0.86*S - 30 (±8)** **r^2 = 0.28**

Supplemental Information.
Vetter, L. et al., Quaternary Science Reviews, 2017.

FIGURE S-7. Calculated $\delta^{18}O_{sw}$ and salinity, Bølling-Allerød Warm Period

Open-ocean
$\delta^{18}O_{sw}$ = 1.85‰
S = 37.65 psu

B_b time slice: 14.00 - 14.01 ka

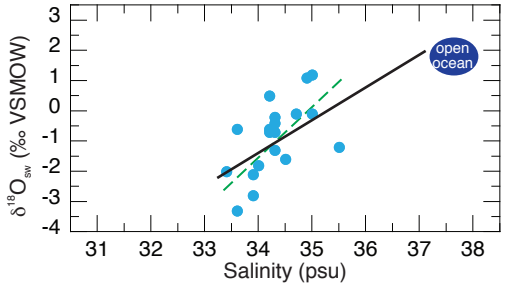

Core interval	Linear regression	Regression including open-ocean value
424 - 424.5 cm 14.00 - 14.01 ka n = 19	$\delta^{18}O_{sw}$ = 1.17*S - 40 (±11) r^2 = 0.32	**$\delta^{18}O_{sw}$ = 0.87*S - 30 (±7)** **r^2 = 0.45**

Open-ocean
$\delta^{18}O_{sw}$ = 1.79‰
S = 37.59 psu

Bølling-Allerød Warm Period, B_c time slice: 13.70 - 13.77 ka

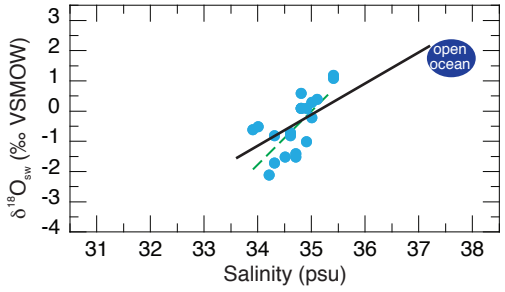

Core interval	Linear regression	Regression including open-ocean value
412 - 412.5 cm 13.70 - 13.71 ka n = 20	$\delta^{18}O_{sw}$ = 1.41*S - 49 (±14) r^2 = 0.43	**$\delta^{18}O_{sw}$ = 0.93*S - 32 (±8)** **r^2 = 0.53**

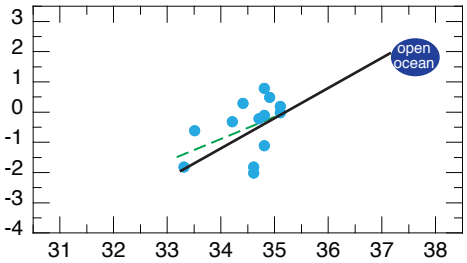

Core interval	Linear regression	Regression including open-ocean value
414 - 414.5 cm 13.75 - 13.77 ka n = 13	$\delta^{18}O_{sw}$ = 0.58*S - 20 (±12) r^2 = 0.18	**$\delta^{18}O_{sw}$ = 0.62*S - 22 (±7)** **r^2 = 0.43**

Supplemental Information.
Vetter, L. et al., Quaternary Science Reviews, 2017.

FIGURE S-8. Calculated $\delta^{18}O_{sw}$ and salinity, Bølling-Allerød Warm Period

Open-ocean
$\delta^{18}O_{sw}$ = 1.93‰
S = 37.73 psu

B_a time slice: 14.61 - 14.65 ka

	Core interval	Linear regression	Regression including open-ocean value
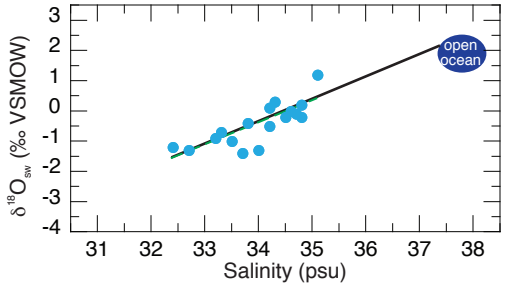	458 - 458.5 cm 14.61 - 14.62 ka n = 17	$\delta^{18}O_{sw}$ = 0.53*S - 18 (±7) r^2 = 0.63	**$\delta^{18}O_{sw}$ = 0.53*S - 18 (±5)** **r^2 = 0.78**
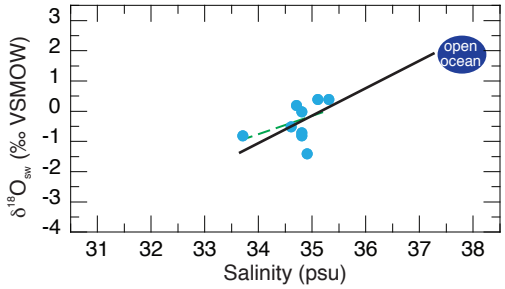	458.5 - 459 cm 14.62 - 14.625 ka n = 9	$\delta^{18}O_{sw}$ = 0.46*S - 16 (±16) r^2 = 0.19	**$\delta^{18}O_{sw}$ = 0.60*S - 21 (±8)** **r^2 = 0.65**
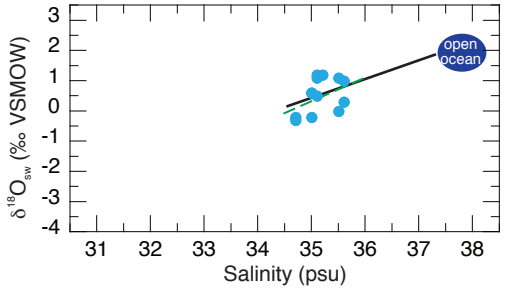	459 - 459.5 cm 14.625 - 14.63 ka n = 13	$\delta^{18}O_{sw}$ = 0.56*S - 19 (±21) r^2 = 0.19	**$\delta^{18}O_{sw}$ = 0.50*S - 17 (±10)** **r^2 = 0.45**
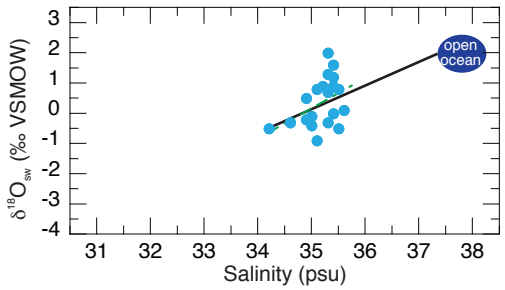	459.5 - 460 cm 14.63 - 14.64 ka n = 20	$\delta^{18}O_{sw}$ = 0.72*S - 25 (±15) r^2 = 0.18	**$\delta^{18}O_{sw}$ = 0.61*S - 21 (±9)** **r^2 = 0.30**

Supplemental Information.
Vetter, L. et al., Quaternary Science Reviews, 2017.

FIGURE S-9. Calculated $\delta^{18}O_{sw}$ and salinity, Heinrich Stadial I

Open-ocean
$\delta^{18}O_{sw}$ = 1.97‰
S = 37.77 psu

H_c time slice: 14.97 - 15.04 ka

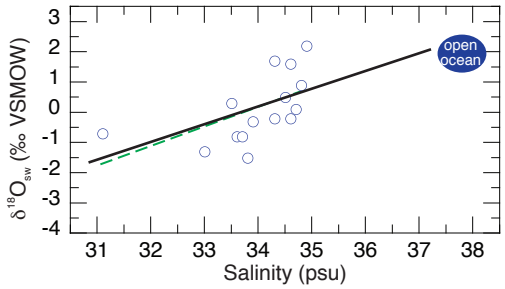

Core interval	Linear regression	Regression including open-ocean value
480 - 481 cm 14.97 - 14.98 ka n = 15	$\delta^{18}O_{sw}$ = 0.58*S - 19 (±6) r^2 = 0.32	**$\delta^{18}O_{sw}$ = 0.50*S - 17 (±5)** **r^2 = 0.43**

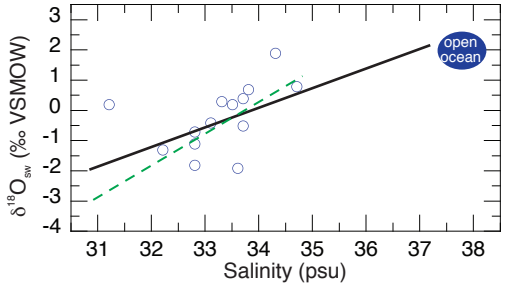

Core interval	Linear regression	Regression including open-ocean value
481 - 482 cm 14.98 - 15.00 ka n = 14	$\delta^{18}O_{sw}$ = 0.78*S - 25 (±9) r^2 = 0.02	**$\delta^{18}O_{sw}$ = 0.51*S - 17 (±5)** **r^2 = 0.34**

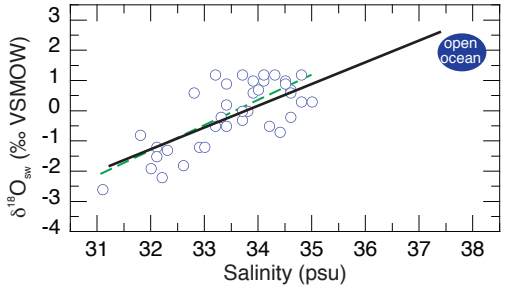

Core interval	Linear regression	Regression including open-ocean value
482 - 483 cm 15.00 - 15.01 ka n = 37	$\delta^{18}O_{sw}$ = 0.64*S - 21 (±4) r^2 = 0.56	**$\delta^{18}O_{sw}$ = 0.58*S - 19 (±3)** **r^2 = 0.58**

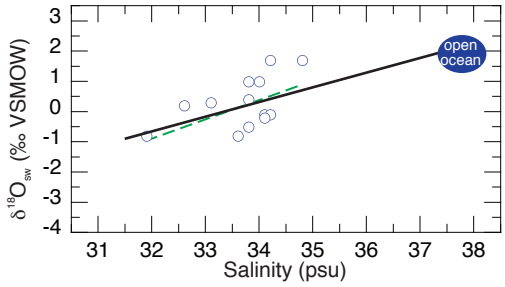

Core interval	Linear regression	Regression including open-ocean value
483 - 484 cm 15.01 - 15.03 ka n = 13	$\delta^{18}O_{sw}$ = 0.50*S - 16 (±10) r^2 = 0.28	**$\delta^{18}O_{sw}$ = 0.39*S - 12 (±5)** **r^2 = 0.44**

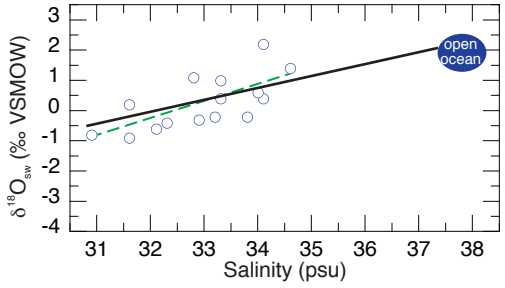

Core interval	Linear regression	Regression including open-ocean value
484 - 485 cm 15.03 - 15.04 ka n = 15	$\delta^{18}O_{sw}$ = 0.42*S - 13 (±5) r^2 = 0.46	**$\delta^{18}O_{sw}$ = 0.35*S - 11 (±4)** **r^2 = 0.54**

Supplemental Information.
Vetter, L. et al., Quaternary Science Reviews, 2017.

FIGURE S-10. Calculated $\delta^{18}O_{sw}$ and salinity, Heinrich Stadial I

Open-ocean
$\delta^{18}O_{sw}$ = 1.99‰
S = 37.79 psu

H_b time slice: 15.39 - 15.54 ka

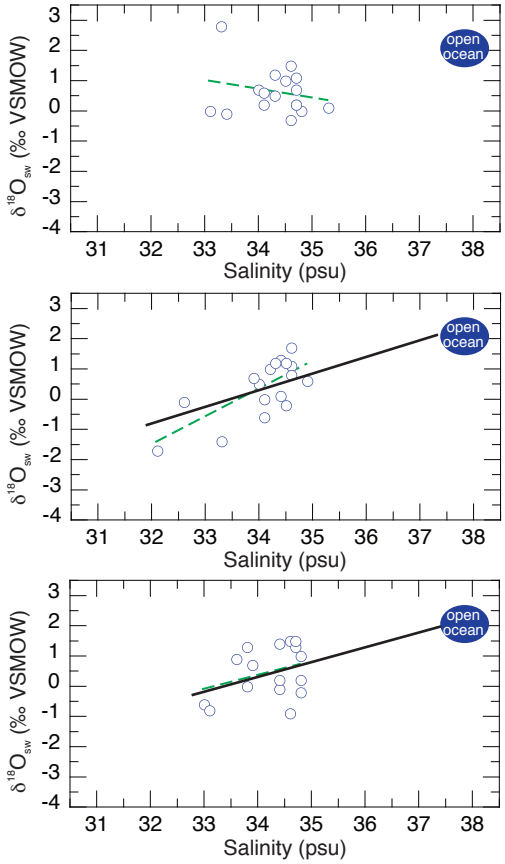

Core interval	Linear regression	Regression including open-ocean value
499 - 500 cm 15.39 - 15.43ka n = 17	$\delta^{18}O_{sw}$ = -0.20*S + 7 (±9) r^2 = 0.05 no relationship	
500 - 501 cm 15.43 - 15.47 ka n =17	$\delta^{18}O_{sw}$ = 0.79*S - 26 (±8) r^2 = 0.50	**$\delta^{18}O_{sw}$ = 0.57*S - 19 (±5)** **r^2 = 0.53**
501 - 502 cm 15.47 - 15.54 ka n = 17	$\delta^{18}O_{sw}$ = 0.39*S - 13 (±9) r^2 = 0.12	**$\delta^{18}O_{sw}$ = 0.39*S - 13 (±6)** **r^2 = 0.27**

Supplemental Information.
Vetter, L. et al., Quaternary Science Reviews, 2017.

FIGURE S-11. Calculated $\delta^{18}O_{sw}$ and salinity, Heinrich Stadial I

Open-ocean
$\delta^{18}O_{sw}$ = 2.04‰
S = 37.84 psu

H_a time slice: 16.79 - 16.86 ka

Core interval	Linear regression	Regression including open-ocean value
544 - 545 cm 16.79 - 16.81 ka n = 7	$\delta^{18}O_{sw}$ = -0.66*S + 23 (±30) r^2 = 0.12 no relationship	
545 - 546 cm 16.81 - 16.82 ka n = 20	$\delta^{18}O_{sw}$ = 0.09*S - 3 (±7) r^2 = 0.01 no relationship	
546 - 547 cm 16.82 - 16.83 ka n = 35	$\delta^{18}O_{sw}$ = 0.13*S - 4 (±6) r^2 = 0.00 no relationship	
547 - 548 cm 16.83 - 16.84 ka n = 15	$\delta^{18}O_{sw}$ = -0.30*S + 11 (±7) r^2 = 0.13 no relationship	
548 - 549 cm 16.84 - 16.86 ka n = 16	$\delta^{18}O_{sw}$ = 0.30*S - 9 (±12) r^2 = 0.05 no relationship	

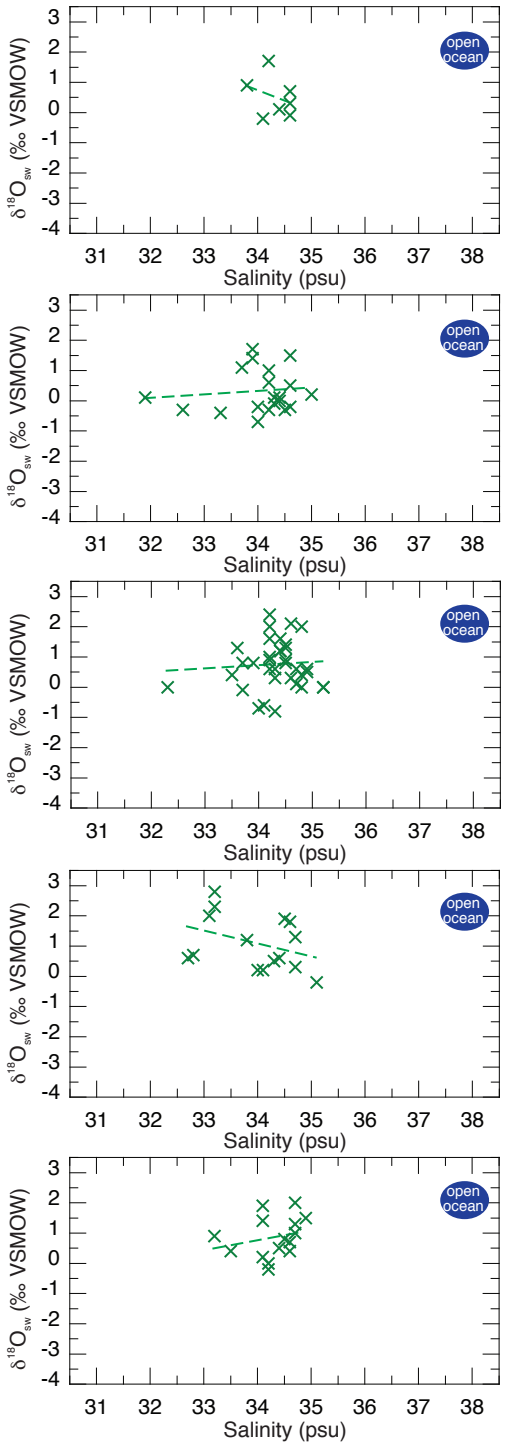

Supplemental Information.
Vetter, L. et al., Quaternary Science Reviews, 2017.

FIGURE S-12. Calculated $\delta^{18}O_{sw}$ and salinity, Early Deglacial

Open-ocean
$\delta^{18}O_{sw}$ = 2.07‰
S = 37.87 psu

ED time slice: 17.34 - 17.43 ka

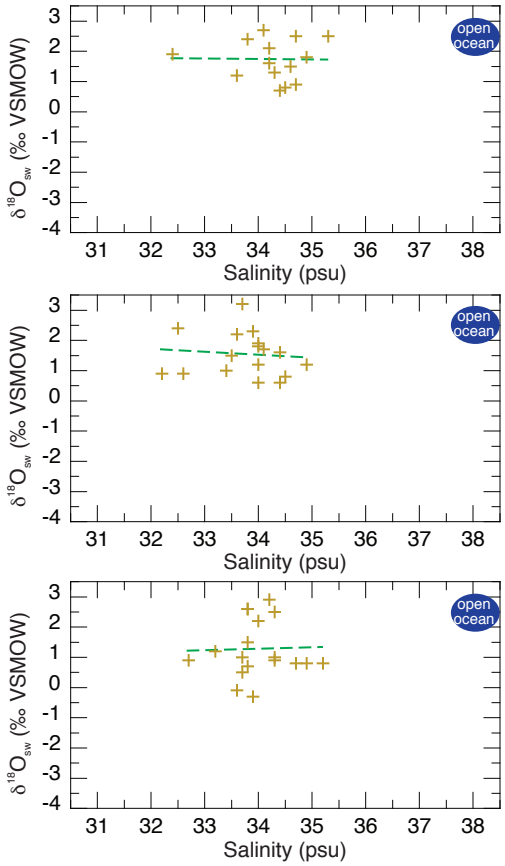

Core interval	Linear regression
581 - 582 cm 17.34 - 17.36 ka n = 13	$\delta^{18}O_{sw}$ = -0.04*S + 3 (±9) r^2 = 0.01 no relationship
582 - 583 cm 17.36 - 17.38 ka n =17	$\delta^{18}O_{sw}$ = -0.10*S + 5 (±7) r^2 = 0.01 no relationship
583 - 584 cm 17.38 - 17.43 ka n = 18	$\delta^{18}O_{sw}$ = 0.04*S - 0.3 (±8) r^2 = 0.01 no relationship

Supplemental Information.
Vetter, L. et al., Quaternary Science Reviews, 2017.

Figure S-13. Evaluating Ba-salinity relationships

Comparison of $\delta^{18}O_{sw}$ vs. salinity reconstructions using measurements from individual *O. universa* from Orca Basin core interval 483-484 cm (15.28-15.30 ka). We follow the methodology presented in the main text (Section 2.2) to convert measured Ba/Ca_{shell} to salinity, using four different basin-specific Ba-salinity relationships (Figure S-2).

The reconstruction using the modern Mississippi-Atchafalaya outflow relationship (blue dots) yields salinity estimates that are consistent with the laboratory-based salinity tolerance range for *O. universa* (Bijma et al., 1990). When we substitute Ba/Ca vs. S relationships from the Ganges-Brahmaputra Delta (red diamonds), the Amazon estuary (green triangles), and the Congo River outflow (purple squares) and perform the same calculations with foraminiferal shell measurements, we obtain considerably lower estimated salinities. Note that the application of different Ba-salinity relationships yields not only different salinity estimates, but also different slopes to the $\delta^{18}O_{sw}$-salinity regression.

For the Congo River, 90% of the data are less than the minimum threshold salinity tolerance range for O. universa of 23-27 psu (Bijma et al., 1990). For the Amazon River relationship (green triangles), >50% of these data would be discarded, and for the Ganges-Brahmaputra relationship (red diamonds) most specimens yield salinities that are within the tolerance range of *O. universa*.

After comparing Ba/Ca-salinity relationships from 4 major rivers on 4 different continents, only the Mississippi and Ganges-Brahmaputra relationships yield salinities for the majority of O. universa that are within the salinity tolerance range for the species. Because there is no logical reason to select a Ba-salinity relationship for a different watershed outside of the region of interest, we are comfortable applying the modern Mississippi-Atchafalaya relationship to interpret the data we have collected on deglacial O. universa in this study.